STUDY OF EQUATORIAL CLUTTER USING OBSERVED AND SIMULATED LONG RANGE BACKSCATTER IONOGRAMS
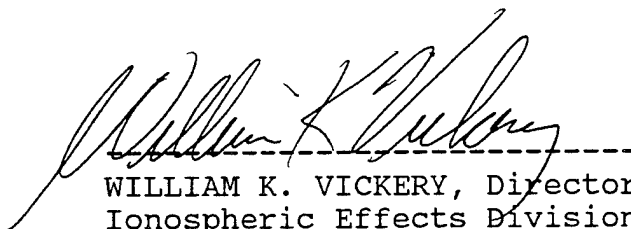
B. S. Dandekar

29 August 1995

19960624 246

PHILLIPS LABORATORY
Directorate of Geophysics
AIR FORCE MATERIEL COMMAND
HANSCOM AIR FORCE BASE, MA 01731-3010

"This technical report has been reviewed and is approved for publication."

Maj Edward Berghorn, Chief
Ionospheric Application Branch

WILLIAM K. VICKERY, Director
Ionospheric Effects Division

This report has been reviewed by the ESC Public Affairs Office (PA) and is releasable to the National Technical Information Service (NTIS).

Qualified requestors may obtain additional copies from the Defense Technical Information Center (DTIC). All others should apply to the National Technical Information Service (NTIS).

If your address has changed, or if you wish to be removed from the mailing list, or if the addressee is no longer employed by your organization, please notify PL/TSI, 29 Randolph Road, Hanscom AFB, MA 01731-3010. This will assist us in maintaining a current mailing list.

Do not return copies of this report unless contractual obligations or notices on a specific document requires that it be returned.

REPORT DOCUMENTATION PAGE

Public reporting burden for this collection of information is estimated to average 1 hour per response, including the time for reviewing instructions, searching existing data sources, gathering and maintaining the data needed, and completing and reviewing the collection of information. Send comments regarding this burden estimate or any other aspect of this collection of information, including suggestions for reducing this burden, to Washington Headquarters Services, Directorate for Information Operations and Reports, 1215 Jefferson Davis Highway, Suite 1204, Arlington, VA 22202-4302, and to the Office of Management and Budget, Paperwork Reduction Project (0704-0188), Washington, DC 20503.

1. AGENCY USE ONLY (Leave blank)	2. REPORT DATE 29 August 1995	3. REPORT TYPE AND DATES COVERED Scientific, Interim

4. TITLE AND SUBTITLE

Study of Equatorial Clutter Using Observed and Simulated Long Range Backscatter Ionograms

6. AUTHOR(S)

B. S. Dandekar

5. FUNDING NUMBERS

PE 62101F
Proj 4643
TA GH
WU 01

7. PERFORMING ORGANIZATION NAME(S) AND ADDRESS(ES)

Phillips Laboratory (GPIA)
29 Randolph Road
Hanscom AFB, MA 01731-3010

8. PERFORMING ORGANIZATION REPORT NUMBER

PL-TR-95-2124
ERP, NO. 1176

9. SPONSORING / MONITORING AGENCY NAME(S) AND ADDRESS(ES)

10. SPONSORING / MONITORING AGENCY REPORT NUMBER

11. SUPPLEMENTARY NOTES

This report will be of interest to operators of the USAF OTH radars.

12a. DISTRIBUTION / AVAILABILITY STATEMENT

Approved for Public release;
Distribution Unlimited

12b. DISTRIBUTION CODE

13. ABSTRACT (Maximum 200 words)

This synoptic study of equatorial clutter used over 6200 long range (8000 nmi) backscatter ionograms from the East Coast Radar System at Bangor, ME, obtained from 1100 to 0600 Local Time during the 22 month period from October 1991 to July 1993. Data were collected in five 7.5° width azimuthal sectors (radar beams 1-6, 1-8, 2-4, 2-8 and 3-5) from 58° T to 170° T. The backscatter clutter signatures can be identified with an equatorial clutter region covering a dip latitude range of ±40°. Equatorial clutter typically begins after sunset and continues through midnight, with a minimum of activity between 1700 and 2200 LT. The clutter range shows some dependence on solar activity with a reduction in range from the radar during low solar activity periods. These data did not show any dependence of clutter on operating frequency or on magnetic activity.

Synthetic backscatter ionograms were generated using the Parameterized Ionospheric Model developed by Anderson at Phillips Laboratory, with the raytrace technique of Jones and Stephenson. The analysis shows that the equatorial dome of the ionosphere favors the chordal mode of reflection from the south side of the dome, which produces horizontal traces as clutter signatures on the backscatter ionograms. The reduction in range at low solar activity is associated with the lowering of the mean height of the ionospheric dome. In beams 2-8 and 3-5 the ionospheric dome structure is associated with the equatorial (Appleton) anomaly. This dome structure geometry favors the chordal mode of reflection.

14. SUBJECT TERMS
OTH radar, Equatorial clutter,
Equatorial ionosphere

15. NUMBER OF PAGES 74

16. PRICE CODE

17. SECURITY CLASSIFICATION OF REPORT	18. SECURITY CLASSIFICATION OF THIS PAGE	19. SECURITY CLASSIFICATION OF ABSTRACT	20. LIMITATION OF ABSTRACT
Unclassified	Unclassified	Unclassified	SAR

Contents

Illustrations

Tables

Acknowledgements

Study of Equatorial Clutter Using Observed and Simulated Long Range Backscatter Ionograms

1. INTRODUCTION

The United States Air Force (USAF) originally deployed two Over-The-Horizon Backscatter (OTH) radars systems for surveillance: 1) East Coast Radar System (ECRS) and 2) West Coast Radar System (WCRS) with operation centers at Bangor, ME, and at Mountain Home, ID, respectively. Because of reduced USSR threat as well as present Department of Defense (DOD) funding limitations, WCRS is in warm storage and only ECRS continues to be operated, routinely collecting normal range (2000 nmi) backscatter ionograms (BSI) in the sectors and segments selected for the radar operation.

For Frequency Modulated Carrier Wave (FMCW) pulsed radar, the wave repetition frequency (WRF) results in the folding of long range signals into the primary-principal range of 2000 nmi producing apparent clutter (unwanted signals) in addition to any clutter actually produced within the primary range. This effect was anticipated and observed in the northern looking sectors and is well known as auroral clutter. During late daytime operation while looking in the equatorward direction the radar observed similar clutter. By collecting special long range (8000 nmi) backscatter ionograms, Jurgen Buchau from Phillips Laboratory correctly identified this clutter to be of equatorial origin, and showed that its diurnal variation was related to the local time, referred to the equatorial region (and not the local time at the transmitter- receiver sites), starting from sunset and continuing through sunrise. Later, the operation of the ECRS radar in Segments II and III (east and south looking paths passing over the equator) routinely detected the equatorial clutter during these time periods. This led to the proposal for the synoptic study of the equatorial clutter through a planned collection of long range (8000 nmi) backscatter ionograms.

In this report we show the signatures of the equatorial clutter sources, present the data base for the study of the equatorial clutter, and discuss the spatial and temporal behavior of the equatorial clutter. The simulation of these long range backscatter ionograms is done to explain the behavior of equatorial clutter. For the synoptic study, ECRS data are used, and for description of clutter signatures, data from both ECRS and WCRS are used.

2. BACKGROUND

Figure 1 shows the location and the coverage areas of both the ECRS and WCRS radars, which typically operate in the frequency range of 5 to 28 MHz. For the ECRS, beams are shown to the antipode point. For these radars, the maximum detection range is 2000 nmi (the ECRS system has been modified to extend the range to 3000 nmi). The aim of the radar is to maintain a barrier width of 500 nmi, typically starting at a distance of 1000 nmi from the transmitter. Each radar covers an azimuth of 180°, as shown in Figure 1, with three 60° segments. For the ECRS, the segments are numbered 1, 2, and 3 starting from north. For WCRS, the segments are also numbered 1, 2, and 3 in the clockwise direction, but starting from south. Due to the asymmetry of the auroral oval in a geographic coordinate system, the ECRS is closer to the oval than the WCRS (note that WCRS is further south than ECRS). Each 60° segment is subdivided into eight 7.5° beams. The boundaries of these beams are also shown in Figure 1, along with the dip equator, ±20° and ±40° dip latitudes. The equatorial anomaly region lies in a narrow region around ± 20° latitude from the dip equator. For the ECRS the northern-most beam is 13000 km (7500 nmi) away from the equator whereas for beam 2-8 this distance is 5900 km (3000 nmi). For WCRS the respective distances are 13500 and 5700 km.

For the radar, the unambiguous range of operation is given by the equation

$$\text{UNAMBIGUOUS RANGE} = 0.5 \ c \ /\text{WRF} \tag{1}$$

where c is the velocity of light and WRF(Hz) is the wave repetition frequency of the radar.

Figure 2 shows the unambiguous ranges for various WRFs for the ECRS beams 2-4, 2-6, and 2-8. At a WRF of 40 Hz the unambiguous range is about 2000 nmi and any clutter from longer ranges is folded into this range. For a WRF of 10 Hz the unambiguous range is 8000 nmi. One of the choices for the mitigation of the long range clutter is to operate the radar at a low WRF.
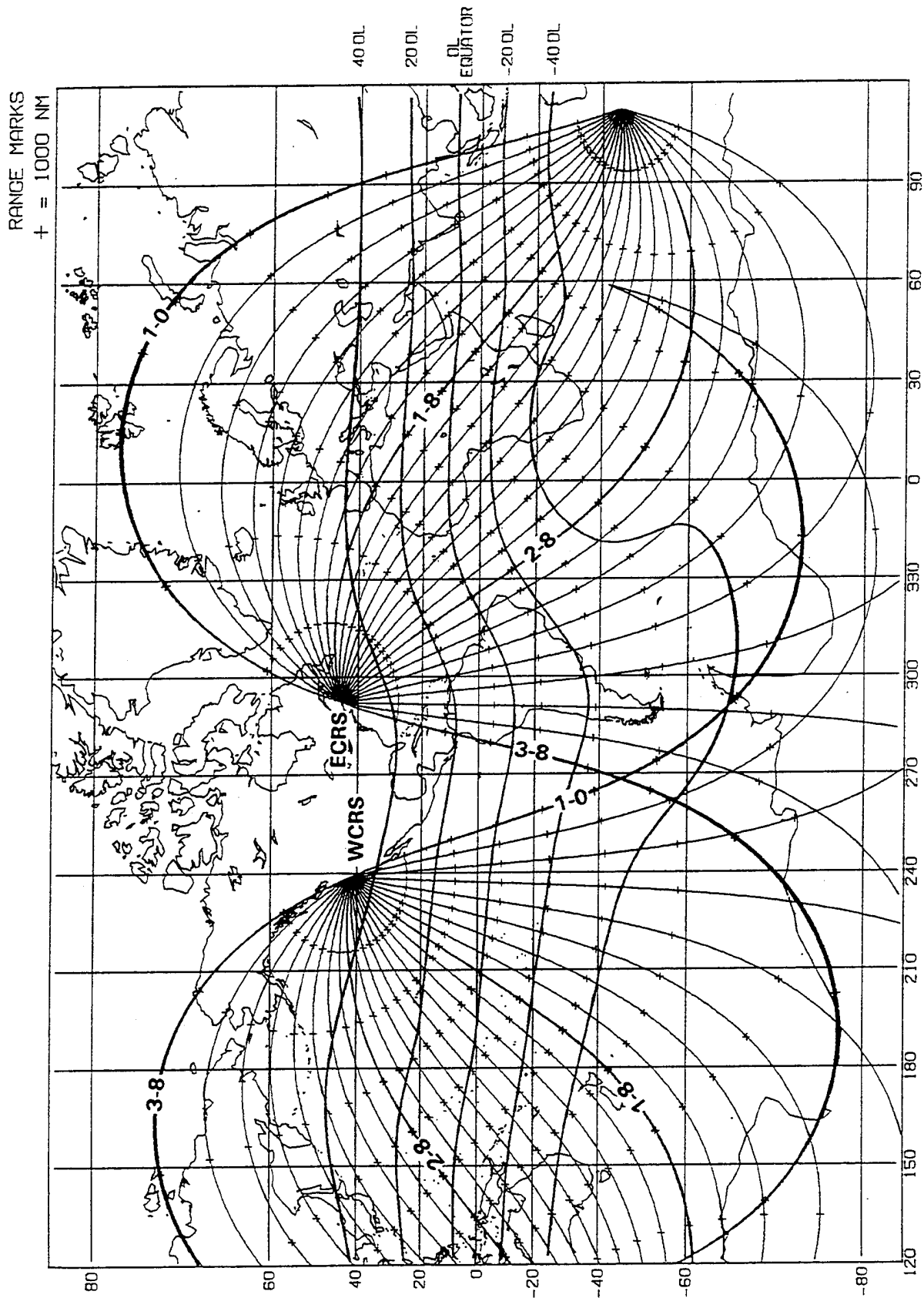
Figure 1. Coverage area of ECRS and WCRS showing the location of various beams.

3
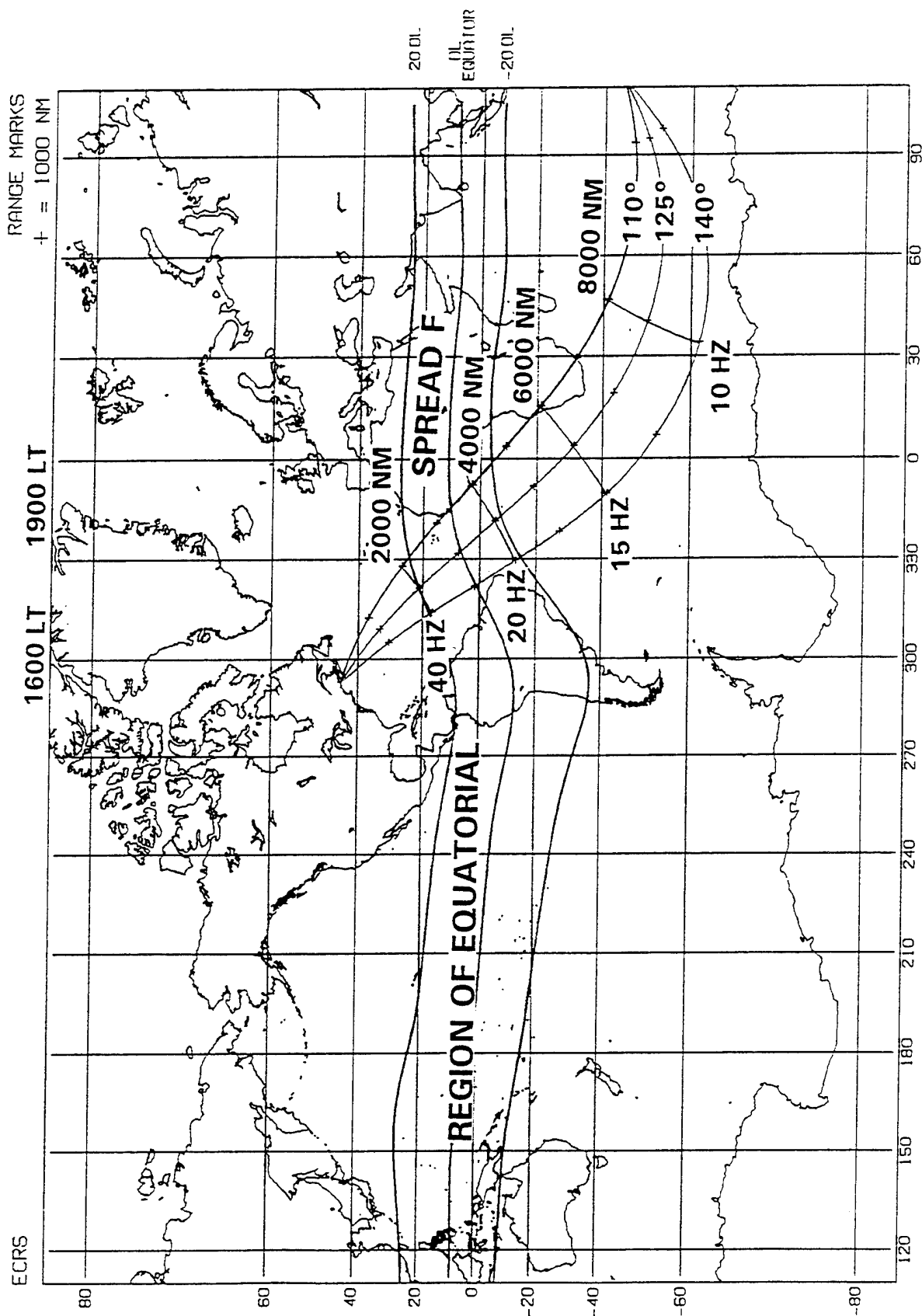
Figure 2. Equatorial effects on the radar due to range folding.

4

Figure 3 shows the Amplitude Range Doppler (ARD) data (from WCRS) which are the primary data used for target detection. The horizontal axis is slant range (delay time divided by 2c) from the radar and the vertical axis is the strength of the received signal. For the upper block the WRF of 40 Hz is used and for the lower block the WRF is 10 Hz; all other radar parameters are the same. Note that for the lower block the unambiguous range (function of WRF) is 8000 nmi whereas for the upper block it is 2000 nmi (see Figure 2). For the lower block the radar dynamic range is 80 dB. (-70 to -150). In the upper block the clutter covers a range of 32 dB (-108 to -140) and the radar is left with the operating range of only 38 dB (-70 to -108). The lower block indicates that there was no clutter up to the range of 1513 nmi. From the upper block the conclusion is that clutter beyond the slant range of 1513 nmi has folded into the unambiguous range of 0-1513 nmi. In the example shown here it was possible to identify the range of the clutter. If the clutter appeared on both WRFs it would not be possible to identify the range of the clutter. In spite of this ambiguity it is still possible to use the ARD data for studying the temporal dependence of the clutter.

From the ARD data, ground clutter to noise (C/N) ratios are routinely computed and displayed for the coverage area of the operating beams of the radar. Figure 4A shows a sequence of such clutter maps for the WCRS. In each map a pair of solid lines mark the sunset terminator. On the display screen the color-shade of these lines tells the operator which side (left or right) is under solar illumination and which side is in darkness (right or left). Note that in Figure 4A the terminator for the first three sections refers to an altitude of 30 km, whereas for the fourth section for 0248 UT the terminator is for an altitude of 300 km above the ground (the corresponding 30 km terminator would be further left of that for 0220 UT in the lower left hand figure). Note also that the region on the left hand side of this double line is in daytime and that on the right hand side the region is entering darkness. The C/N contours for the region show that the ratio decreases (radar performance progressively deteriorates) as the sunset transition progresses over the region. Conversely an increasing C/N is seen in Figure 4B for the sunrise transition. In Figure 4B the region on the right hand side is in daytime. In the two lower sections the double line is absent because it is on the left hand side and outside of each of these frames. It is shown later that this regular behavior is associated with the phenomenon of equatorial clutter.
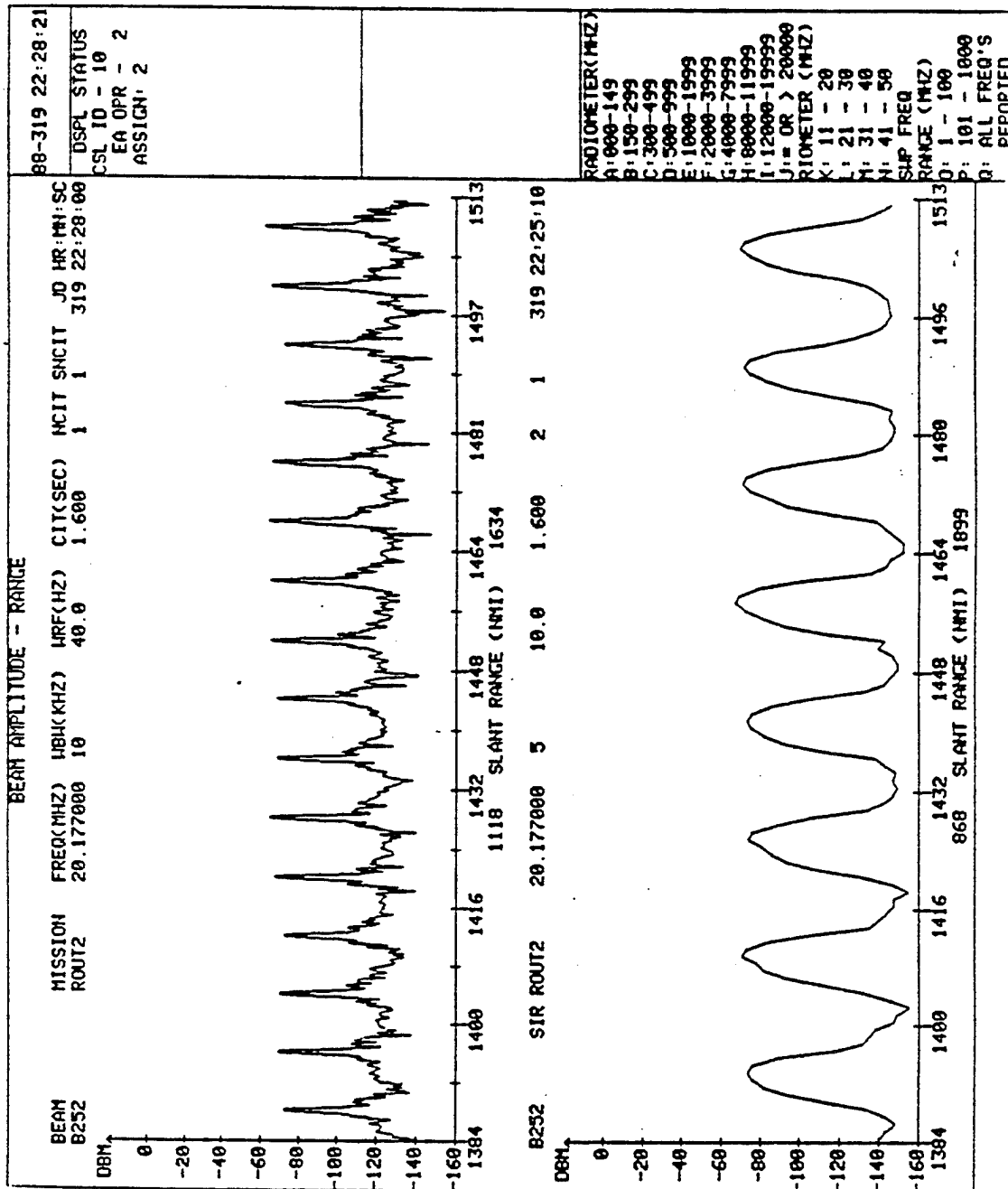
Figure 3. Amplitude Range Data (ARD) for 40 and 10 Hz WRF showing the resolution of clutter.
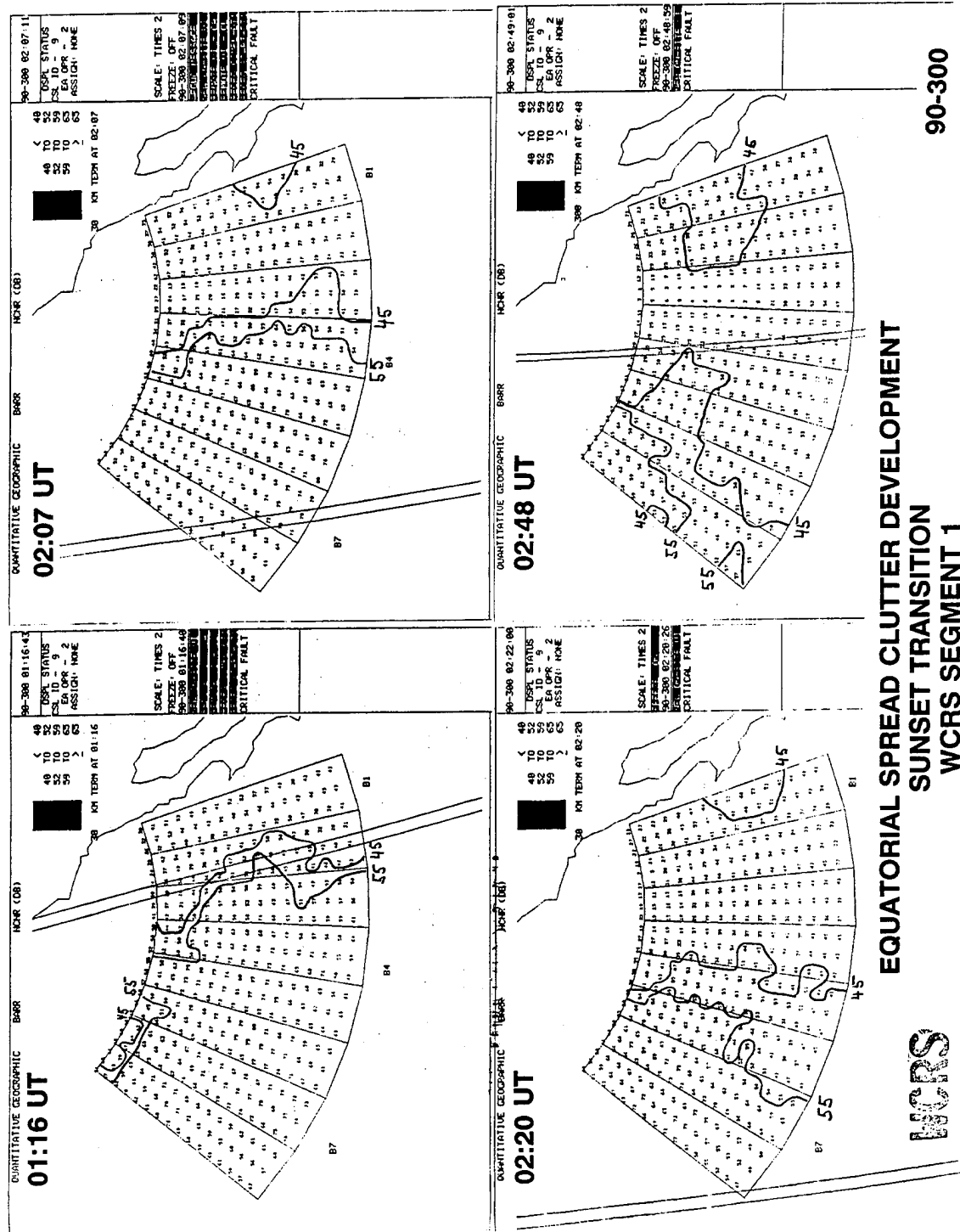
Figure 4A. Equatorial spread clutter development at sunset transition in WCRS segment 1.

RECOVERY FROM EQUATORIAL SPREAD CLUTTER
SUNRISE TRANSITION
WCRS SEGMENT 1

90-300

Figure 4B. Recovery from equatorial spread clutter at sunrise transition in WCRS segment 1.

8

In Figures 5A-5C we see the use of long range backscatter ionograms (BSI to 8000 nmi) for frequency management and identification of the clutter sources. The location of the clutter seen on the BSI can be marked on a range-beam map as shown in Figure 1. The marked location can then be associated with ionospheric features such as the northern and southern auroral oval, midlatitude region, equatorial anomaly, etc. Figure 5A shows a backscatter ionogram for beam 2-2, day 90-139 (year and the day number) at 0426 UT for the WCRS radar. The two traces starting in the lower left hand corner show the ground backscatter for the first and second hop modes. The barrier marker shows that for this beam the radar operation frequency was 14.6 MHz. The ground signatures at 7500 and 10,000 km when mapped on the range map of Figure 1, indicate that these features originate in the southern anomaly and in southern midlatitudes respectively. Figure 5B presents a BSI for beam 2-4, day 90-233 at 1406 UT showing features associated with the northern and southern anomalies. Figure 5C for WCRS for beam 2-2, day 90-299 at 1426 UT shows features associated with the southern anomaly, the southern midlatitudes and with the southern auroral oval. We use the BSIs collected from ECRS for the study of the equatorial clutter.

3. DATABASE

For the synoptic equatorial clutter study, ECRS operators were requested to routinely collect long range (8000 nmi) backscatter ionograms (BSI) on paper (hard copy) on a non-interference basis. The data were routinely collected for beams 1-6, 1-8, 2-4, 2-8, and 3-5 (data collection started in October 1991 with beams 1-8, 2-8, 3-5; beams 1-6 and 2-4 were added starting in July 1992). The plan was to collect two BSIs per beam per hour. A list of the data collection is presented in Table 1. The table presents the year and month in the first two columns. The next column presents the number of days for which data are available for that month. The following 24 columns present the number of backscatter ionograms available for each hour of that month for all the five beams listed above. The last two columns present the total number of ionograms for the given month and the Zurich sunspot number observed for the month. The line at the bottom presents the number of BSIs available for each hour over the whole period. The table shows that data collection started in October 1991. The last month of data used for the study is July 1993. During this period of 22 months, a total of 6254 BSIs were collected on 376 days for the equatorial clutter study. The data coverage is good from 1400 to

9

Figure 5A. Backscatter ionogram for WCRS for beam 2-2 showing the locations of clutter from southern anomaly and southern midlatitude regions.

BACKSCATTER IONOGRAM

POWER ATTENUATION   3 DB
SWEEP RATE   25 KHZ/SEC
BARRIER GND RNG START   510 NMI
----IN USE R-F TRACE SECTOR 5 TIME
- - -ALTN R-F TRACE SECTOR   TIME

SEGMENT 2   SOUNDING SECTOR 2
SECTORS 1 2 3 4 5 6 7 8 UTILIZE
R-F TRACE FROM SECTOR 5
RADAR CLP OVERLAY   B222 1132
TERRAIN FEATURE(S)

SEG 2 SEC 2 90-139 0426 UT

SOUTHERN MIDLATITUDE (?)
~ 10,000 km

SOUTHERN ANOMALY
~ 7500 km

SLANT RANGE (NMI)

8000
6400
4800
3200
1600
0

FREQUENCY (MHZ)
6   10.0   14.0   18.0   22.0   26

90-139 04:45:00

Figure 5B. Backscatter ionogram for WCRS for beam 2-4 showing locations of clutter from northern and southern anomaly regions.

11

BACKSCATTER IONOGRAM

POWER ATTENUATION   6 DB
SWEEP RATE   25 KHZ/SEC
BARRIER GND RNG START 1200 NMI
---- IN USE R-F TRACE SECTOR 1 TIME 90-299 14:14:37
-- -- ALTH R-F TRACE SECTOR   TIME

SEGMENT 2   SOUNDING SECTOR 2
SECTORS 1 2   UTILIZE
R-F TRACE FROM SECTOR   1
RADAR CLP OVERLAY   B222
TERRAIN FEATURE(S)

90-299 14:41:12

DSPL STATUS
CSL ID - 9
  EA OPR - 6
ASSIGN: NONE

SCALE: FULL
FREEZE: OFF
90-299 14:25:14

REMOTE UI
IONO PARAMETERS

STA NO.   70265
COLLEGE
SNDG DATE 299
SNDG TIME 13:00

FOF2   3.4 MHZ
HMF2   240 KM
FOF1   MHZ
HMF1   KM
FOE   0.6 MHZ
HME   110 KM
FOES   MHZ

W 3000 FACTR

FMIN   2.6 MHZ
QUALIFIER 2
FBES   MHZ
TIME - 14:39:04

SOUTHERN AURORAL OVAL SECTOR 22
~ 14,000 km

SOUTHERN MIDLATITUDE (?)
~ 8600 km

SOUTHERN ANOMALY
~ 7000 km

SEG 2 SEC 2 90-299 1426 UT

B222

SLANT
RANGE
(NMI)

8000
6400
4800
3200
1600
0

6   10.0   14.0   18.0   22.0   26
FREQUENCY (MHz)

Figure 5C. Backscatter ionogram for WCRS for beam 2-2 showing locations of clutter from southern anomaly, southern midlatitude, and southern auroral oval regions.

12

Table 1. ECRS Data Base For Synoptic Study Of Equatorial Clutter

YR	MN	DY	UT																								NOB	SSN
---	---	---	12	13	14	15	16	17	18	19	20	21	22	23	00	01	02	03	04	05	06	07	08	09	10	11	---	---
91	10	25		1			2	4	4	11	6	12	16	13	16	10	6	2	6	3							112	142
91	11	16		1	12	14	21	23	29	39	37	33	18	12	1	4	2	2									248	138
91	12	17	3	4	9	13	15	15	22	19	22	26	27	22	20	19	24	16	11	5	2				1	1	296	132
92	1	21				12	9	21	29	36	39	34	34	22	16	15	9	15	12	11		13	14	4			360	124
92	2	12	2	9	8	13	18	12	10	13	19	9	5	3	8	5	5	1									140	115
92	3	9	1	1	7	6	14	13	7	13	17	15	8	5	4	3	1	1									118	108
92	4	21	7	7	4	3	18	26	34	28	38	31	32	8	4	4	4	3		1		1	4		3	3	255	103
92	5	18	2	3	4	4	7	5	16	20	15	23	9	6	5	9	7	3		4		5		5			138	100
92	6	12			4	3	3	7	3	2	6	1	1	5	5	6	3	1									64	97
92	7	19	3	1	13	32	81	69	82	58	73	67	83	6	1	6	3	4	5	2	5		3			1	670	91
92	8	4		31	27	4	11	16	24	11	14	19	10	2													111	84
92	9	18	21			32	26	42	31	9	6	7	6	2	35	8											238	80
92	10	23	2				1	7	47	38	49	54	28	28		8											298	76
92	11	17					3	8	12	20	25	33	26	3													130	74
92	12	20			1	1	6	12	37	33	38	40	34	16	7	6	1				4						245	73
93	1	19				3	34	45	97	89	60	64	95	22	7	10											509	71
93	2	20		1	28	20	29	25	24	23	20	11						23	27	35	20	28	33	37	12		396	69
93	3	22				5	36	37	68	68	51	59	42	20				5	11	21	13	10	14	18	5		462	67
93	4	20		8	43	70	37	63	71	61	41	63	63	11	1	9	12	22	16	21	13	23	6				654	63
93	5	18				15	38	49	40	41	67	45	56	40	34	2	2										429	60
93	6	15		1		14	31	21	30	27	25	37	13	17	5												221	56
93	7	10	9	14	21	35	38	34	30	37	22	8	4													8	260	54
	22	376	50	81	181	283	447	547	748	690	695	680	622	279	165	121	88	83	84	92	65	80	70	68	22	13	6254	

UT - Universal Time, YR - year, MN - month, DY -no. of days, NOB - no. of backscatter ionograms, SSN - Zurich sun spot number.

13

0200 UT. The data starts with a high sunspot number of 142 and ends with a low sunspot number of 54, thus providing coverage of both high and low solar activity periods. For this analysis 1 August 92 is used as the line of demarcation between the high and low solar activity periods.

The data coverage by beams and months is presented in Table 2. Note that for the months of August and September, data are available only for the year 1992. A look at the remaining data in the table shows that although the data distribution with respect to months is not uniform, the overall distribution with respect to the beams (last line at the bottom) is reasonably uniform. This allows us to study clutter behavior in different regions covered by the respective beams.

4. ANALYSIS

The clutter data are found to be better organized in a dip latitude and local time system of coordinates, and this system is used here. The local time periods of data coverage in this system of coordinates is shown in Figure 6. In Figure 6 the left hand side curves show the start of observations for various beams, and the numbers at the top of the curves show the start time in universal time (UT). The right hand side curves show the end of observations. Each beam starts at the transmitter and covers a range of 8000 nmi. Note that beam 3-5 looks at essentially the same local time, whereas beam 1-6 looks through a time interval of 9 hours in LT. The observations cover a time period from 11 LT to 06 LT with a dip latitude range of +55° to -50°. This figure, in combination with data from Table 1, shows a good data coverage for the sunset transition and a scanty coverage for the sunrise transition.

Because the beams cover different local time intervals (seen in Figure 6) the data from Table 1 are sorted according to beams for studying the percent occurrence of clutter and its dependence on universal time. The results are presented in Table 3. The first two columns in Table 3 list the number and the look azimuth of the beam. The third column presents the total number of observations available for that beam. This column shows that data collection is reasonably uniform over the beams. The fourth column presents a percent occurrence of clutter. The column is divided into two parts. The number in the first part of the column provides percent occurrence of clutter seen in that beam from all the BSIs for that beam. The fourth column shows that the percent occurrence varies over the beams. This variation could be misleading because the hourly coverage is not reasonably uniform,

14

Table 2. Long Range Backscatter Observations by Beams

| SEG-SECTOR	1-6			1-8			2-4			2-8			3-5		
MON\YEAR	91	92	93	91	92	93	91	92	93	91	92	93	91	92	93
JANUARY		10	106		150	112		22	120		60	120		118	51
FEBRUARY			83		50	82		6	102		42	97		42	32
MARCH		8	96		27	94		4	111		52	110		27	51
APRIL		12	142		64	146		23	142		66	128		90	96
MAY		5	85		47	86		1	107		55	105		30	46
JUNE			34		17	35			75		31	61		16	16
JULY		97	83		107	86		124	44		132	45		110	2
AUGUST		28			27			14			20			22	
SEPTEMBER		55			55			13			10			105	
OCTOBER	1	56			60		11	60			54		100	68	
NOVEMBER		25		64	19			20		85	14		99	52	
DECEMBER	10	43		87	32		24	72		109	52		66	46	
TOT BY YR	11	339	629	151	655	641	35	359	701	194	588	666	265	726	294
TOT BY BEAM	979			1447			1095			1448			1285		
TOT OBSERVATIONS	6254														
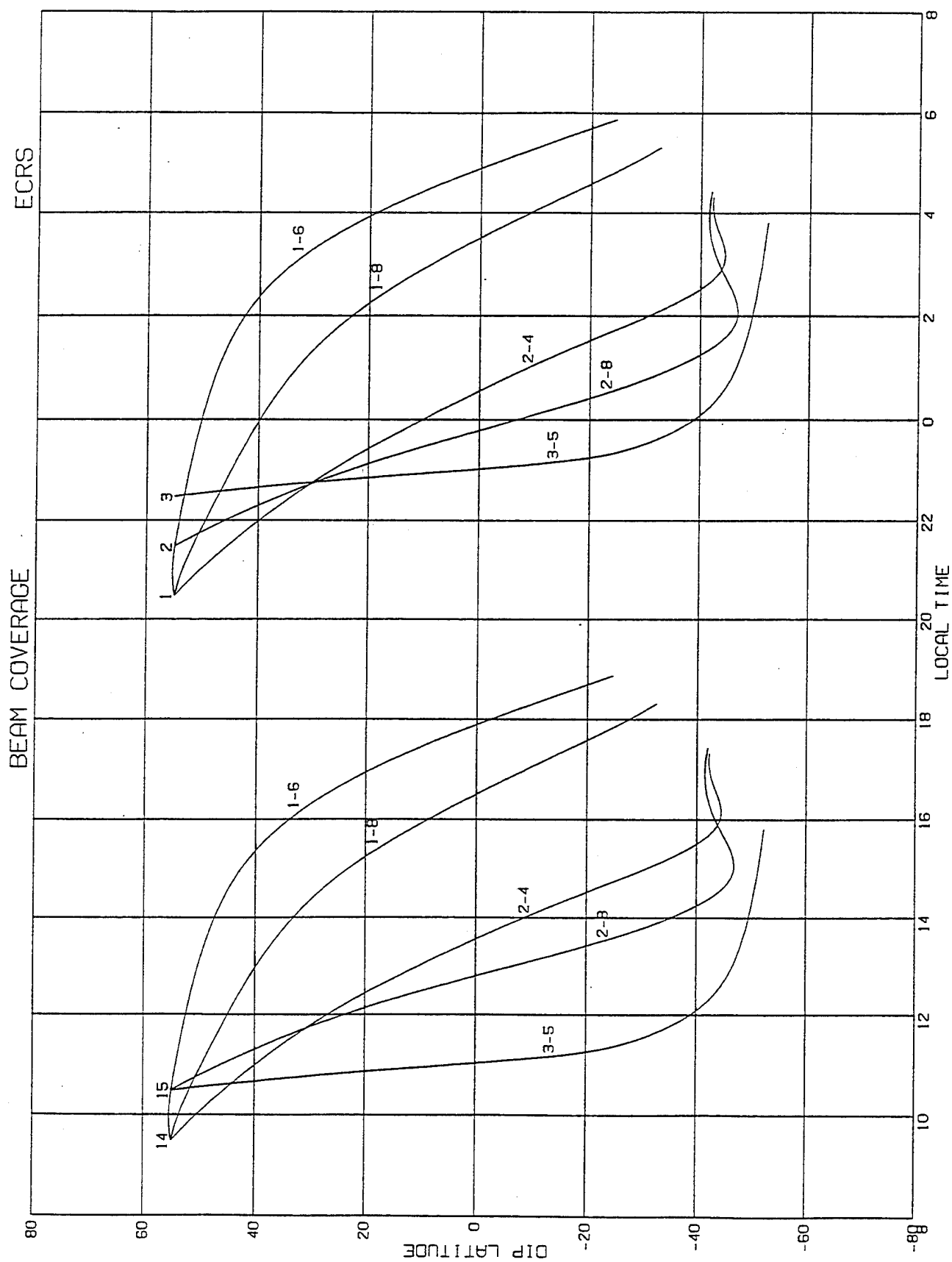
Figure 6. Local Time and Dip Latitude window of data collection.

16

Table 3. Hourly Occurrence of Clutter in Various Beams

BEAM	AZM	NO OF BSI	%	OCCUR	CLUTTER OCCURRENCE (>50%) IN UT INTERVALS									
					18	19	20	21	22	23	00	01	02	03
3-5	170.25	1285	42	72				50	63	82	93	70	71	
2-8	132.75	1448	60	74		53	63	78	86	91	79	76	72	70
2-4	102.75	1095	60	70		54	74	81	85	87	91	66	43	50
1-8	72.75	1447	44	63				65	61	56	59	75	59	
1-6	57.75	979	35	54				61	58	53	51	50	50	

and consists of different look directions. Also, the number of observations in each time interval and the time intervals (Figure 6) covered by the respective beams are different. This variation could be misleading when the hourly coverage is not reasonably uniform. Furthermore, the conclusion based on these observations would be worse if there are more hourly observations for the daytime hours when the equatorial clutter is normally absent and few for the night time hours when the clutter is normally present. To remove this ambiguity, the second part of the fourth column also presents the average for the hours for which occurrence of clutter was greater than 50 percent. A look at the time dependence (in the last column) shows that clutter is a regular phenomenon in beams 3-5, 2-8, and 2-4 starting at the sunset transition period and continues for at least 6 hours through the evening and midnight hours (there are not enough data for late night and sunrise hours). In beams 1-8 and 1-6, which look over a wide time interval, the clutter effect is certainly present but does not appear as strong because of the spread of these data over a longer time interval. Overall the table shows that equatorial clutter is a regular phenomenon starting at local sunset and continuing through the sunrise hours. In beams 3-5, 2-8, and 2-4 at certain hours the clutter is greater than 90 percent showing that equatorial clutter is a regular feature in these time intervals.

The observed clutter traces shown in Figures 5A-5C for October 1991 - July 1992 (high solar activity with average sun spot number =135) and for August 1992 - July 1993 (low solar activity with average sun spot number=75) are all presented in dip latitude and local time coordinates in Figures 7A and 7B respectively. In Figures 5A-5C showing the backscatter observations, the ordinate shows the slant range, which represents the time delay.
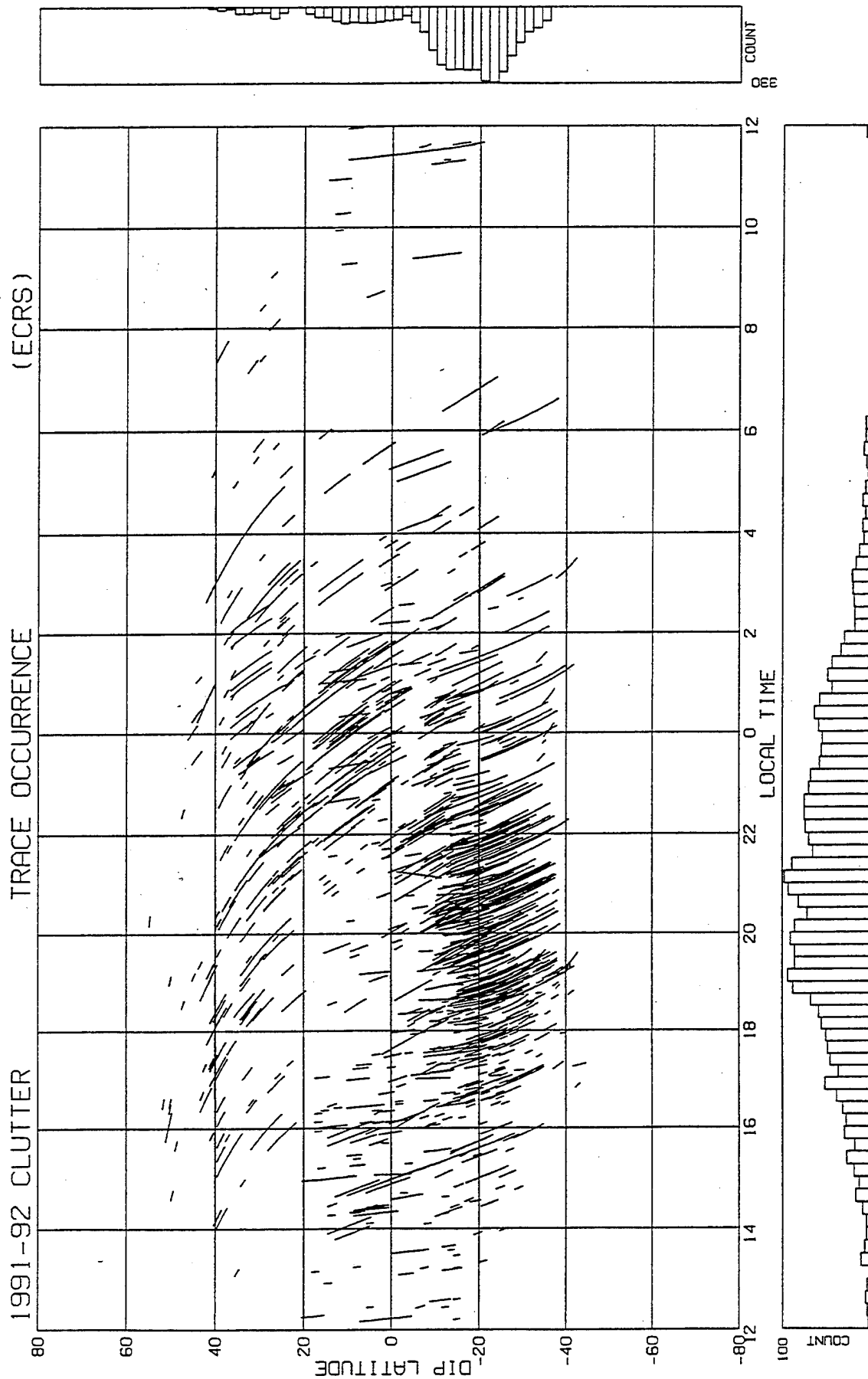
Figure 7A. Location of observed clutter for ECRS for high solar activity (SSN = 135) period (November 1991 to July 1992).
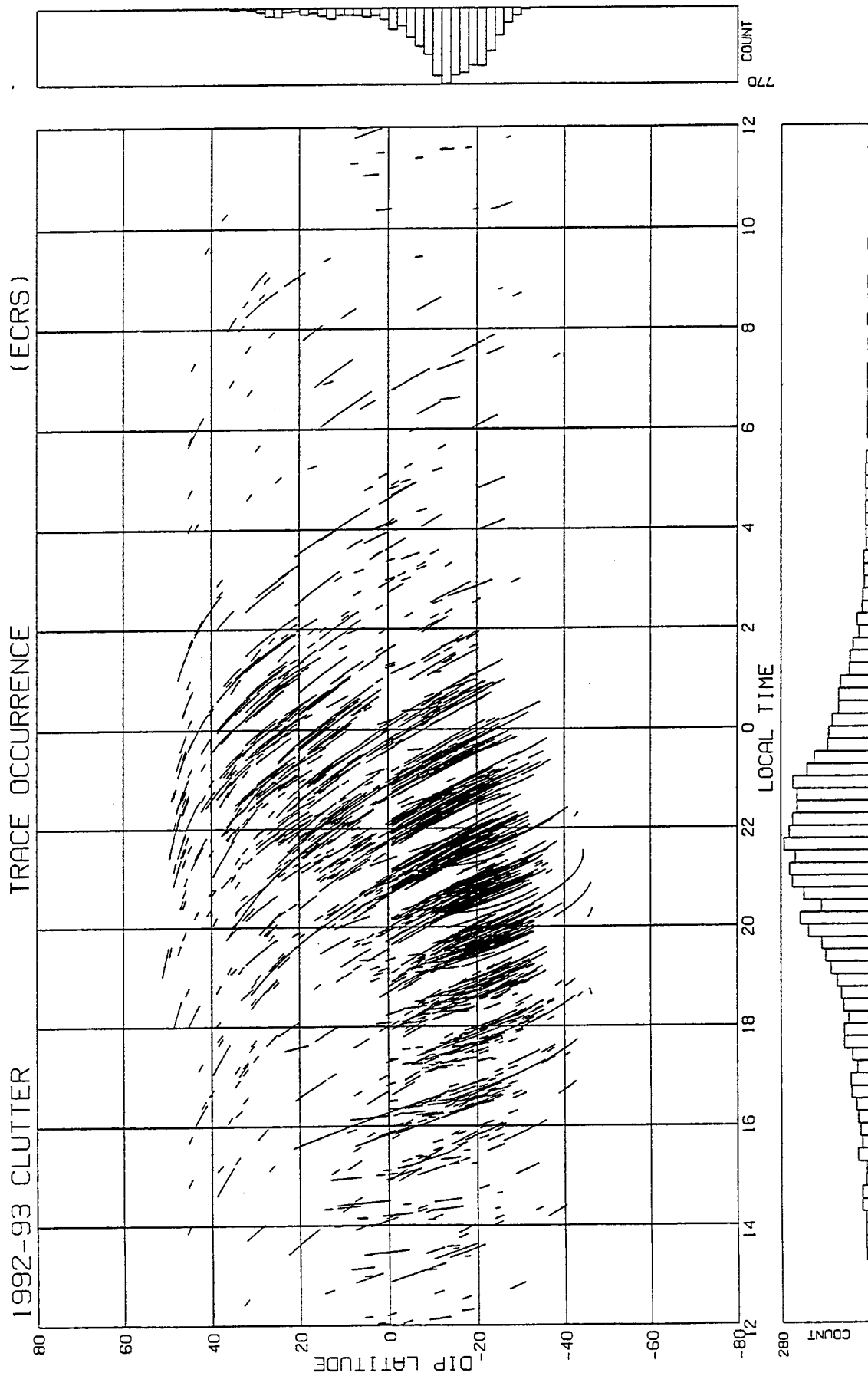
18

Figure 7B. Location of observed clutter for ECRS for low solar activity (SSN=75) period (August 1992 to July 1993).

19

Figures 7 and 8 show ground range plotted in dip latitude and UT coordinates. The slant range is converted to ground range by the use of an average correction of 6 percent (discussed later). In Figure 7A for high solar activity, the clutter lies symmetrically around the dip equator and covers ±40° range of dip latitudes. The clutter begins around 1400 LT and is seen up to 0400 LT. The clutter is most frequent in -12° to -34° dip latitudes: the seat of the southern anomaly. The clutter occurrence is lower in the region of ±20° dip latitudes for 1700 to 2200 LT. In Figure 7B for low solar activity, the distribution is similar to that of Figure 7A for high solar activity, but is shifted northward by 10° and the window of reduced activity near the dip equator is from 1600-2000 LT. In both these figures the clutter from the southern anomaly region is most frequent.

Data shown in Figures 7A and 7B are divided into seasons of high and low solar activity periods to see if there are seasonal and solar activity based differences in the behavior of the clutter. The data are grouped in four seasons 1) Fall (August 7 to November 6), 2) Winter (November 7 to February 4), 3) Spring (February 5 to May 6), and 4) Summer (May 7 to August 6). These are presented in Figures 8A-8H. In Figures 8A and 8B for the fall season, the appearance of additional clutter occurring from the northern anomaly during the low solar activity period, compared to that with high solar activity period, is an artifact of more and better time coverage of observational data in the latter period. This can be confirmed by comparing the count and percent histograms at the bottom of Figures 8A and 8B. Figures 8C to 8F present the data for winter and spring seasons. For both of these seasons the location of the clutter moves 10° northward from -30° to -20° when moving from high to low solar activity periods, and the window, the period of reduced occurrence near the magnetic equator, lengthens by two hours. Also in Figures 8D and 8F the northward shift of clutter steadily increases from 2000 to 0000 LT. Figures 8G and 8H show the clutter behavior for summers of 1992 and of 1993. No significant change in the clutter behavior with respect to solar activity is seen in the summer season.

To test the effect of solar activity on the range and frequency dependence of the clutter, data for the corresponding seasons and corresponding hours are compared. Each group for a given season is split into two parts to study the effect of high and low solar activity on the behavior of the equatorial clutter. These data are presented in Tables 4A to 4E for the five beams. If the number of hourly observations is less than six the corresponding data are deleted from these tables. A look at
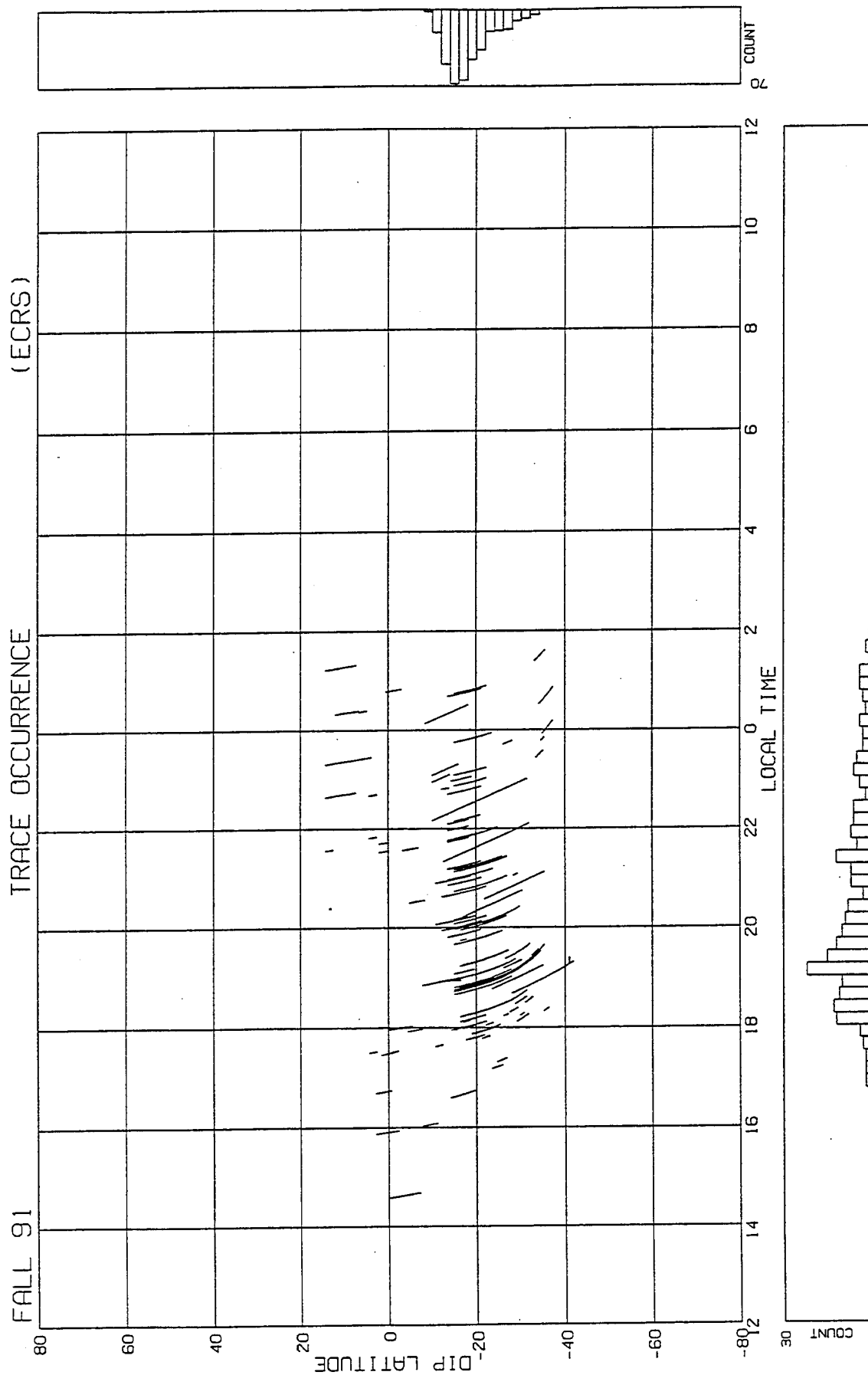
20

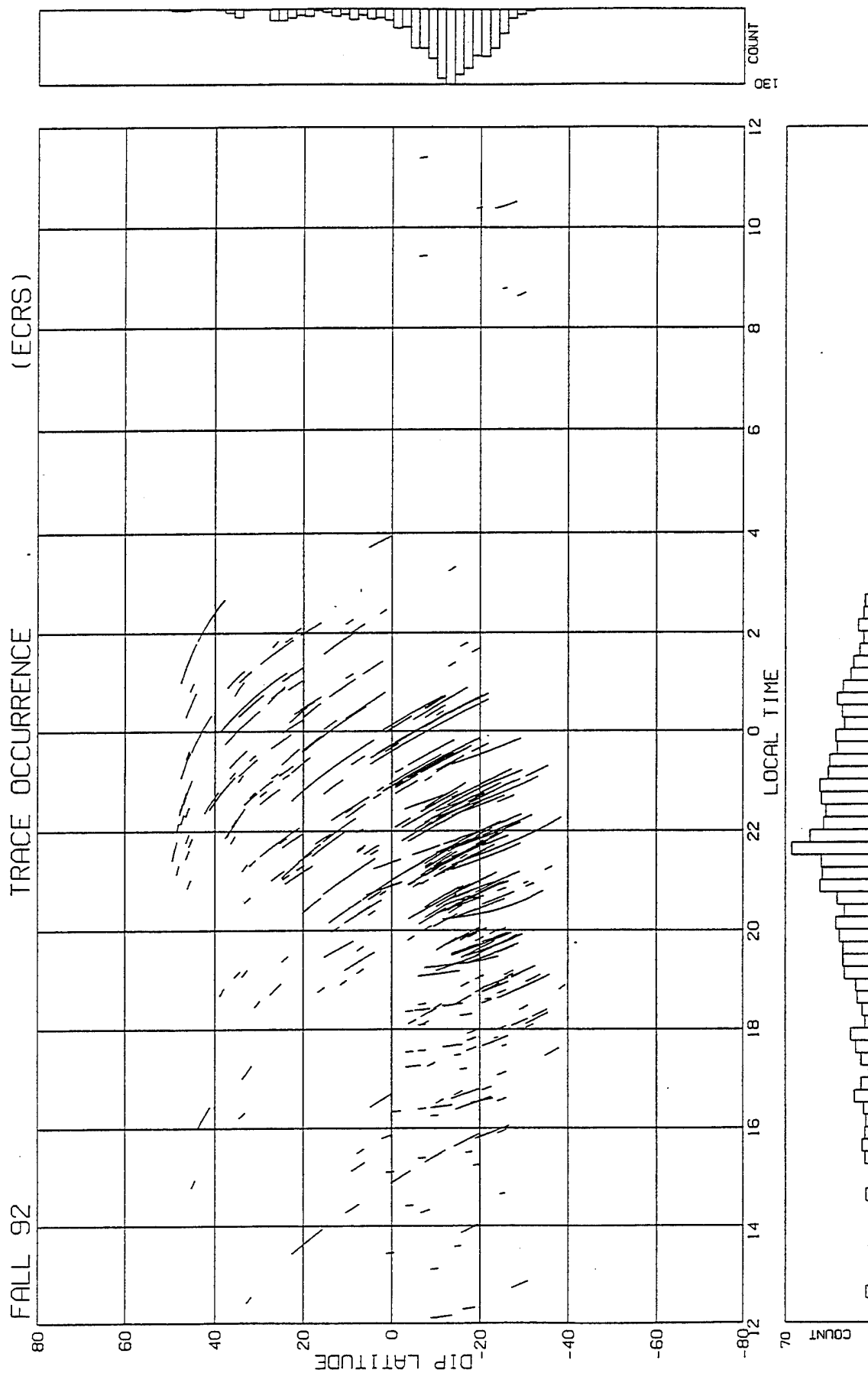Figure 8A. Clutter observed for fall of 1991 (high solar activity period).

21

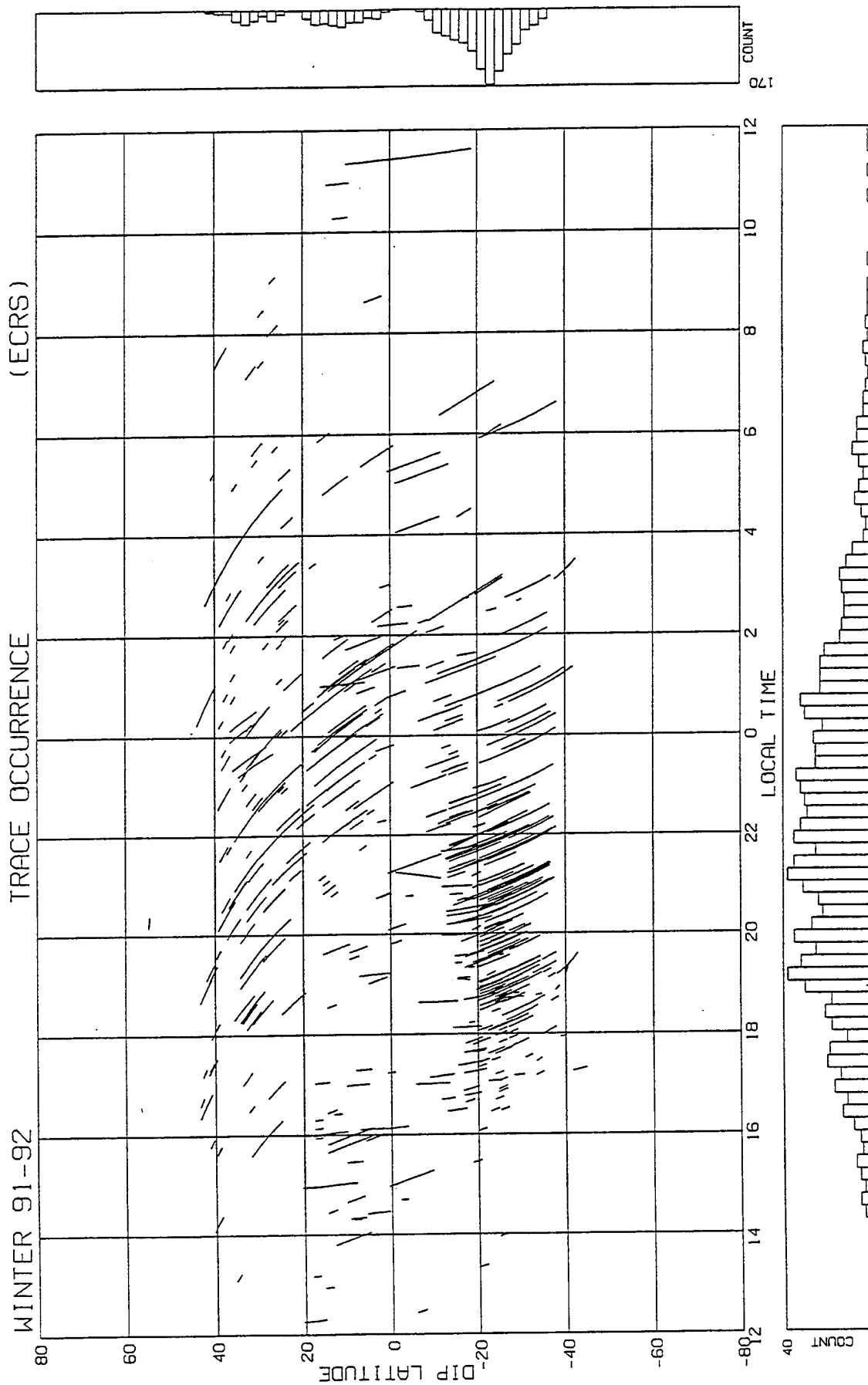Figure 8B. Clutter observed for fall of 1992 (low solar activity period).

22

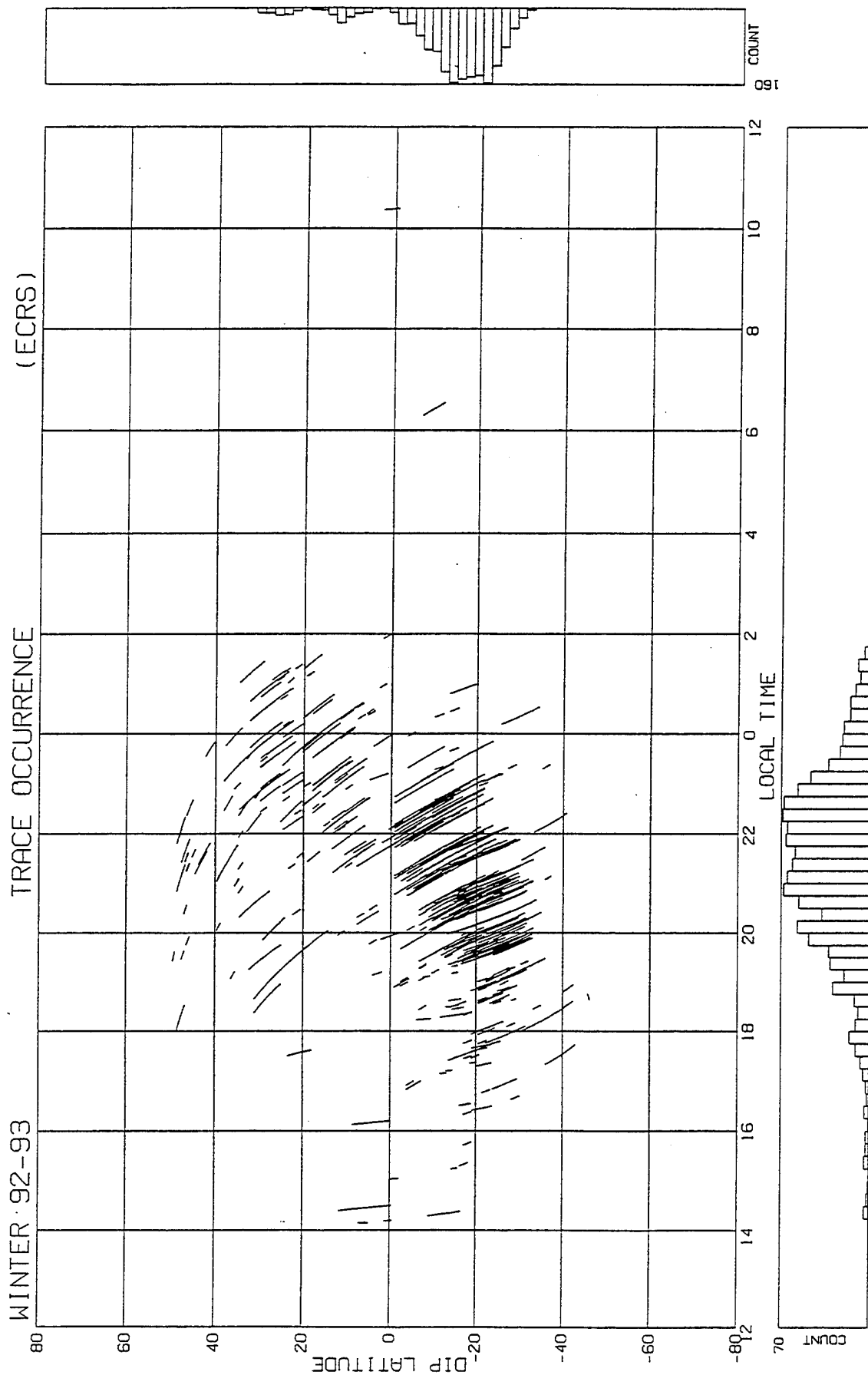Figure 8C. Clutter observed for winter of 1991-92 (high solar activity period).

23

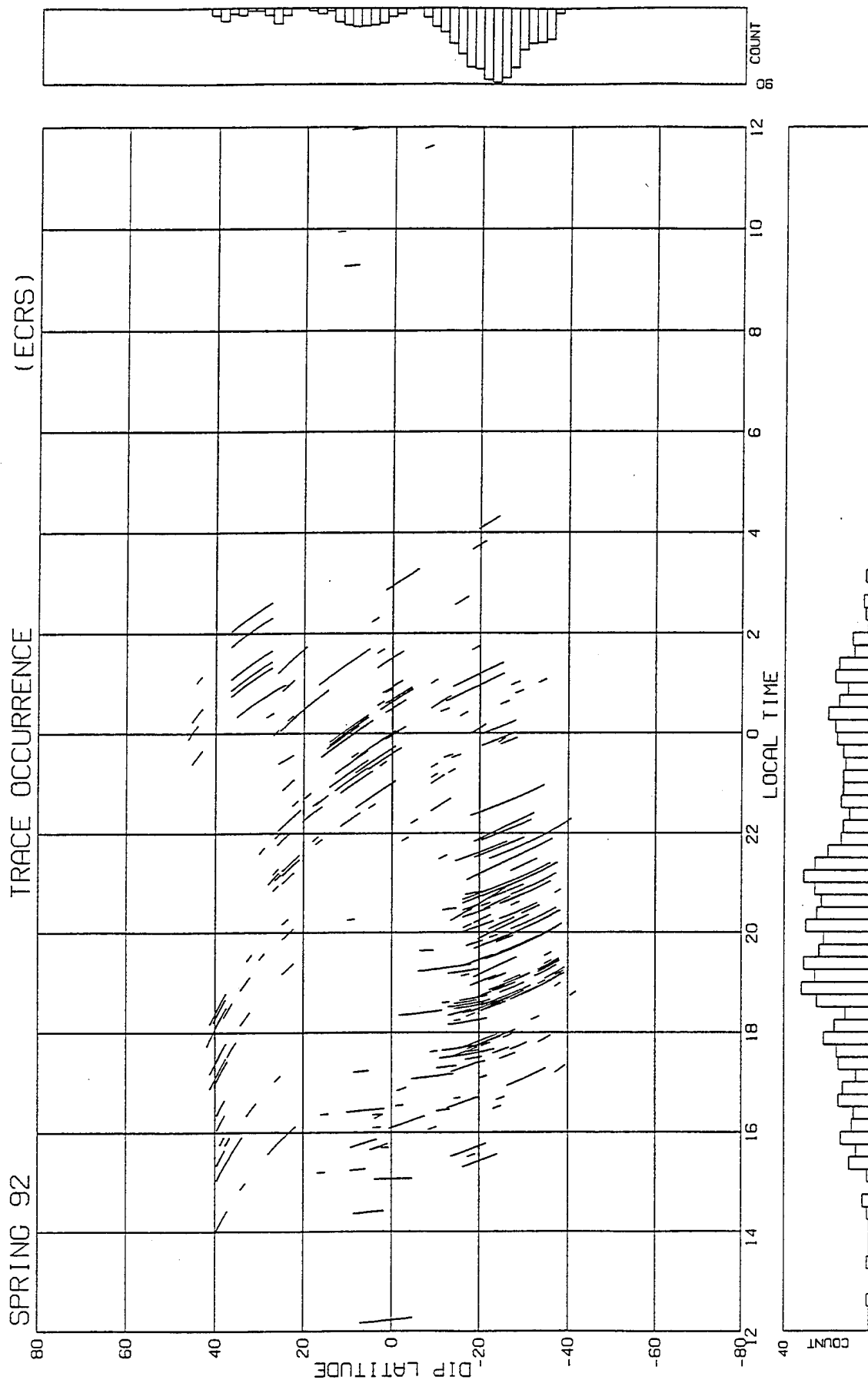Figure 8D. Clutter observed for winter of 1992-93 (low solar activity period).

Figure 8E. Clutter observed for spring of 1992 (high solar activity period).
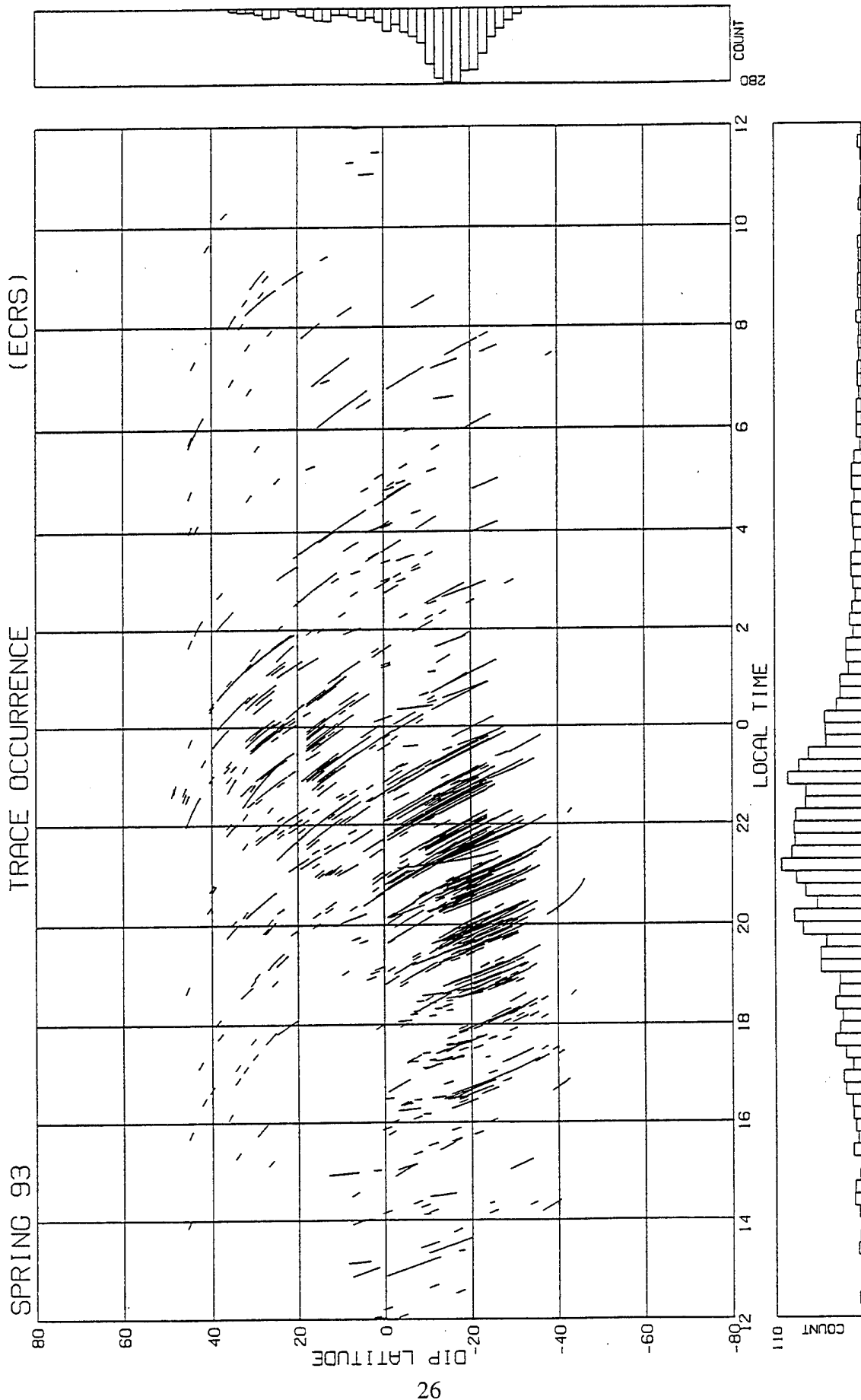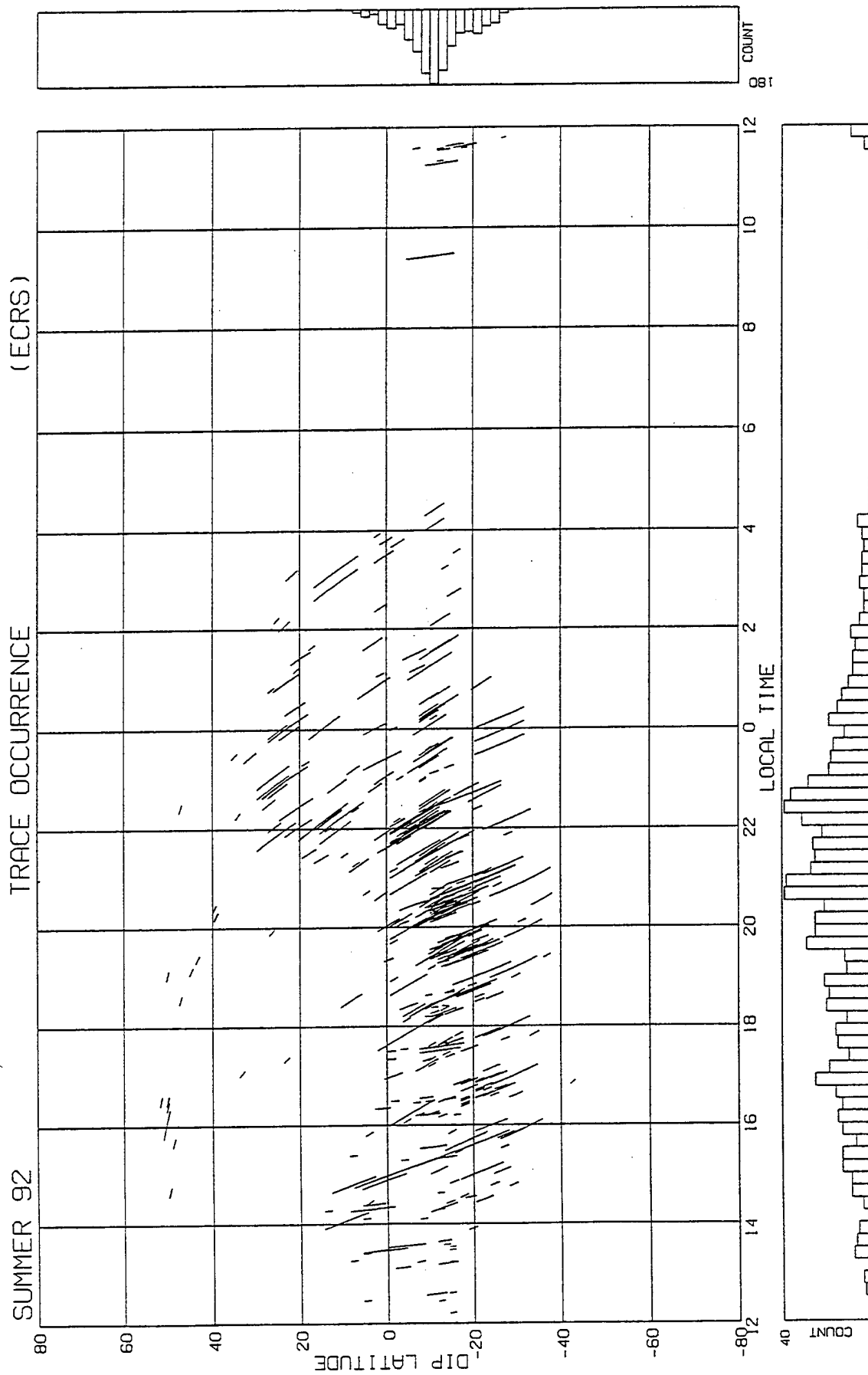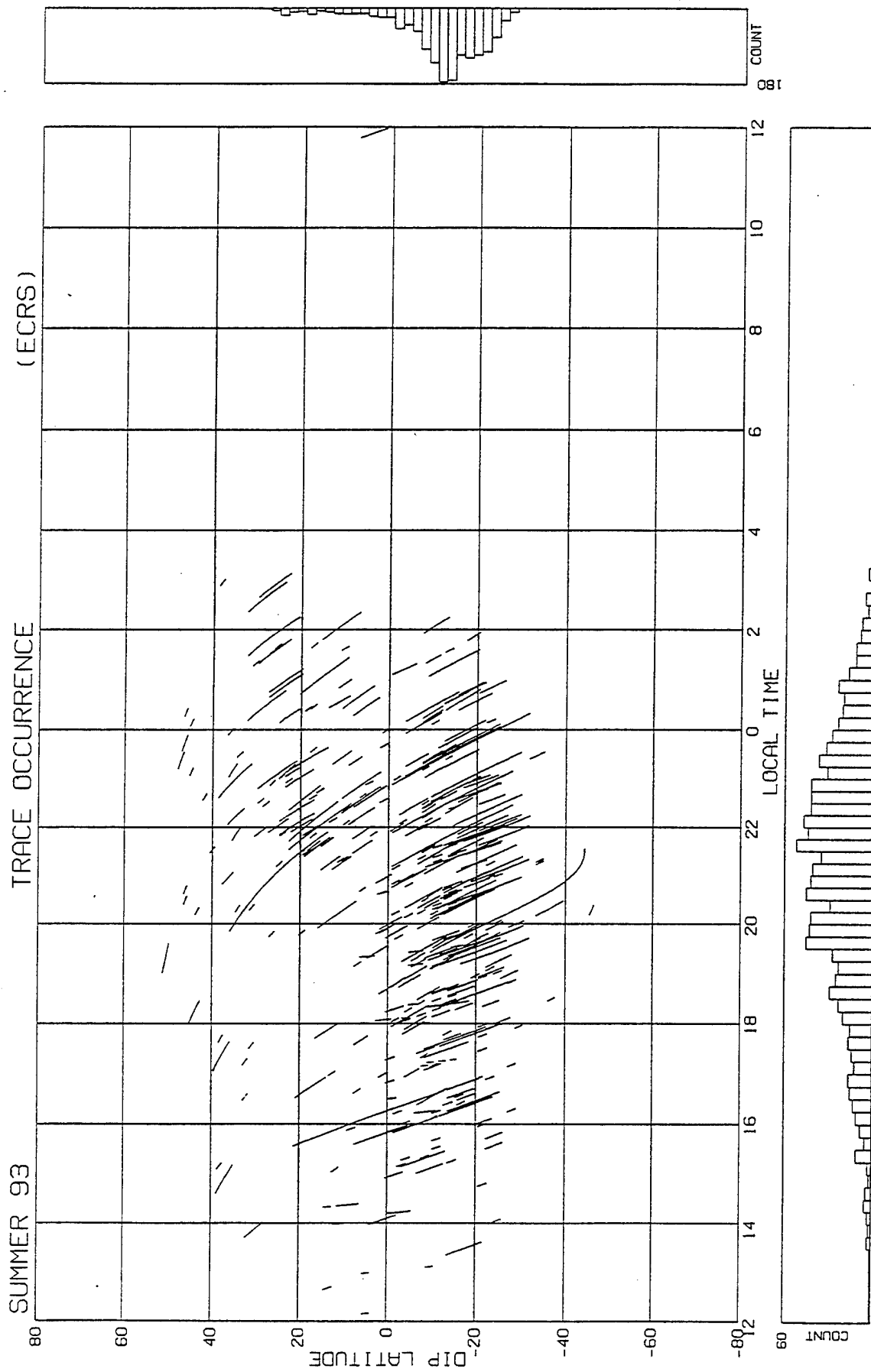
25

Figure 8F. Clutter observed for spring of 1993 (low solar activity period).

26

Figure 8G. Clutter observed for summer of 1992 (high solar activity period).

27

Figure 8H. Clutter observed for summer of 1993 (low solar activity period).

Table 4 A. Hourly Observations at ECRS for Beam 1-6 by Season and Level of Solar Activity

SEASONS								
	FALL		WINTER		SPRING		SUMMER	
SOLAR ACTIVITY								
UT	HIGH	LOW	HIGH	LOW	HIGH	LOW	HIGH	LOW
13-14		10						
14-15		8				13		8
15-16		10				19		12
16-17		11		9		19	12	18
17-18		17		13		30	9	18
18-19		20		33		35	13	20
19-20		13		31		31	9	18
20-21		16		27		27	17	17
21-22		19		24		30	12	13
22-23		12		31		25	13	14
23-00		6		7		11		14
00-01		6						7
01-02								
02-03								
03-04						7		
04-05						10		
05-06						16		
06-07						12		
07-08						16		
08-09						14		
09-10						14		

Table 4 B. Hourly Observations at ECRS for Beam 1-8 by Season and Level of Solar Activity

	SEASONS							
	FALL		WINTER		SPRING		SUMMER	
	SOLAR ACTIVITY							
	HIGH	LOW	HIGH	LOW	HIGH	LOW	HIGH	LOW
13-14		9			6			
14-15		8			6	11		6
15-16		9	8		8	19		13
16-17		10	14	7	14	19	14	17
17-18		16	12	11	17	30	12	18
18-19		22	18	29	16	36	18	23
19-20		13	23	29	21	30	19	21
20-21		16	25	24	25	27	19	19
21-22		17	30	24	16	32	19	12
22-23		12	29	31	11	27	14	13
23-00		6	18	9		11		15
00-01		10	12					6
01-02			16					
02-03			18					
03-04			12			9		
04-05			16			10		
05-06			10			16		
06-07			8			10		
07-08			11			16		
08-09			12			12		
09-10						15		

30

Table 4 C. Hourly Observations at ECRS for Beam 2-4 by Season and by Level of Solar Activity

	SEASONS							
	FALL		WINTER		SPRING		SUMMER	
	SOLAR ACTIVITY							
UT	HIGH	LOW	HIGH	LOW	HIGH	LOW	HIGH	LOW
14-15						16		
15-16						23	7	9
16-17				10		26	16	11
17-18			6	15		27	16	21
18-19		14	10	30		42	16	16
19-20		8	7	31		36	13	20
20-21		9	4	30		30	15	27
21-22		15	6	32		34	14	21
22-23		13		44		30	19	20
23-00		7		8		8		19
00-01		9						11
01-02								7
02-03								
03-04						14		
04-05						14		
05-06						18		
06-07						10		
07-08						15		
08-09						13		
09-10						11		
10-11						7		

Table 4 D. Hourly Observations at ECRS for Beam 2-8 by Season and by Level of Solar Activity

	SEASONS							
	FALL		WINTER		SPRING		SUMMER	
	SOLAR ACTIVITY							
	HIGH	LOW	HIGH	LOW	HIGH	LOW	HIGH	LOW
14-15			8			17		
15-16			12			19	9	10
16-17			10	8	16	25	22	11
17-18			15	13	10	27	21	16
18-19		16	17	28	16	38	33	18
19-20		10	20	29	17	38	13	22
20-21		8	29	20	27	32	20	21
21-22		15	21	33	17	30	22	15
22-23		10	24	33	16	27	23	18
23-00		9	24	12	7	7		19
00-01		8	18					13
01-02			16			9		
02-03			17					
03-04			13				12	
04-05			7				12	
05-06							15	
06-07							14	
07-08							14	
08-09							14	
09-10							14	

Table 4 E. Hourly Observations at ECRS for Beam 3-5 by Season and by Level of Solar Activity

	SEASONS							
	FALL		WINTER		SPRING		SUMMER	
	SOLAR ACTIVITY							
UT	HIGH	LOW	HIGH	LOW	HIGH	LOW	HIGH	LOW
12-13		11						
13-14		10			6			
14-15		15	7		9	7		
15-16		18	14		8	16	12	
16-17		21	15	9	15	24	15	
17-18		30	21	11	18	25	22	6
18-19		35	34	28	15	24	15	7
19-20	8	22	40	21	23	28	12	3
20-21	9	21	38	24	23	21	14	6
21-22	11	16	35	25	19	18	17	6
22-23	18	10	21	14	13	11	10	
23-00	13		12					
00-01	14		9					
01-02	11		6					
02-03	7		7					
03-04								
04-05	6							

Tables 4A-4E shows: 1) reasonably good data are available for 1600 to 0000 UT, 2) good coverage in beams 1-8, 2-4, 2-8, and 3-5 for comparing equatorial clutter for high and low solar activity periods for spring, summer and winter seasons, 3) good coverage in beam 1-6 for low solar activity only, for all seasons. For determining the difference of clutter behavior between high and low solar activity periods only data from common time intervals are compared.

Before the corresponding data are compared, the distance along each beam to reach the equatorial anomaly region consisting of the dip latitude range of ±20° is computed and listed in Table 5. A typical skip distance is about 1200 nmi. A look at Table 5 shows that beam 2-8 is the best for exploring the equatorial clutter, followed by beams 3-5 and 2-4. The northern beams 1-8 and 1-6 barely reach the northern tip (20° dip latitude) of the equatorial anomaly. Thus beams 3-5, 2-8, and 2-4 are able to provide data for the study of the equatorial clutter, whereas beams 1-8 and 1-6 will provide more information on midlatitude clutter than on equatorial clutter.

Table 5. Distance(nmi) from the Transmitter to
the Specified Point for Various Beams

BEAM NO	DISTANCE (nmi) TO LAT.		
	20°	0°	-20°
1-6	5200	6500	7700
1-8	4200	5600	7000
2-4	2400	3700	5000
2-8	1900	3000	4200
3-5	2000	3300	4800

Figure 9 presents slant range (from the radar) of clutter vs relative frequency of occurrence for beam 3-5 for the fall season. The upper and lower sections are for high and low solar activity periods respectively. Each section lists the beam number, the UT interval covered, number of observations (BSIs) providing the data and the number of clutter events observed. Note that the number of clutter events is larger than the number of BSIs, indicating that each BSI may have several clutter events at different ranges (for example see Figures 5A-5C). In Figure 9, a look at the
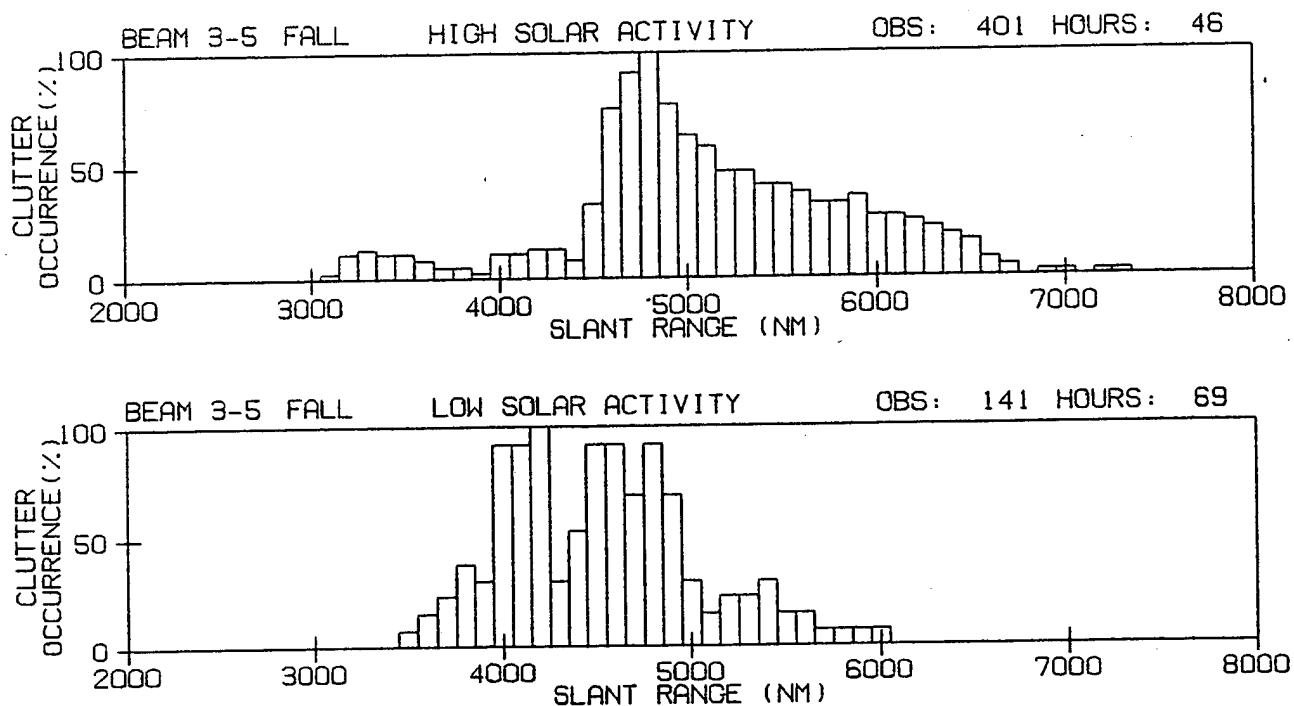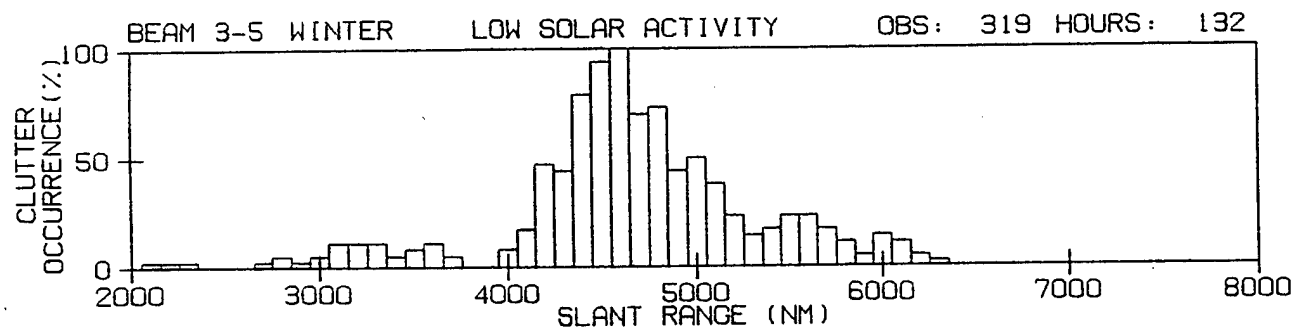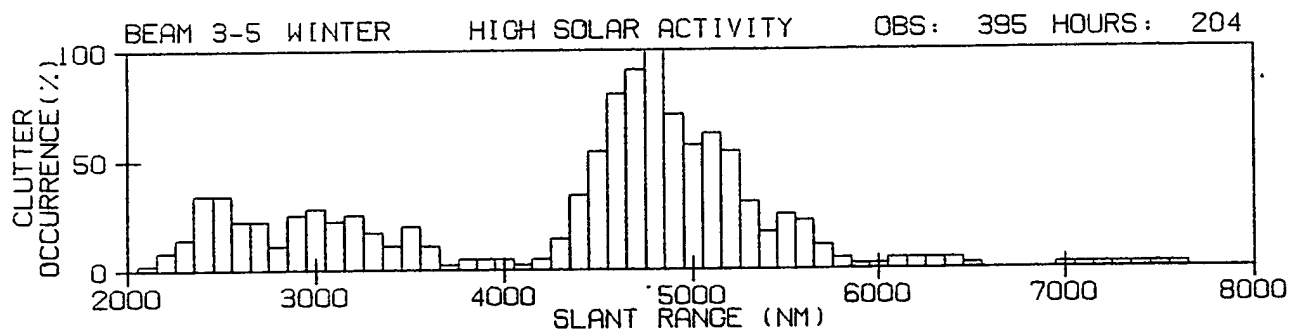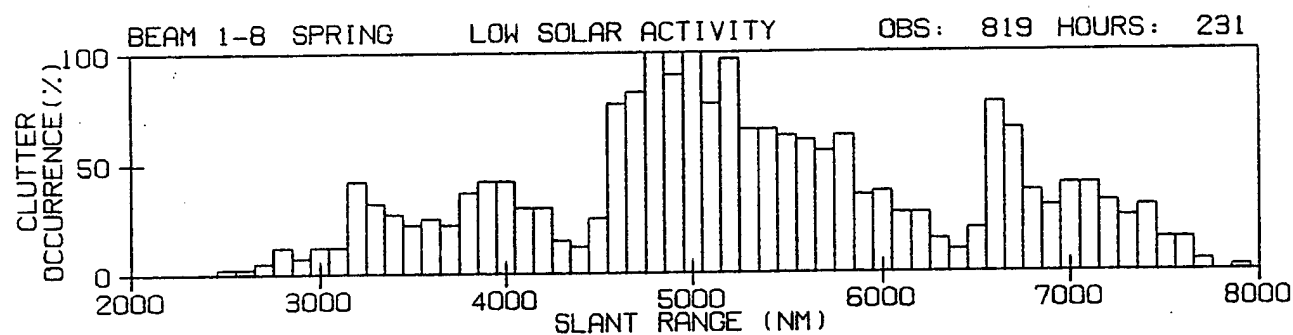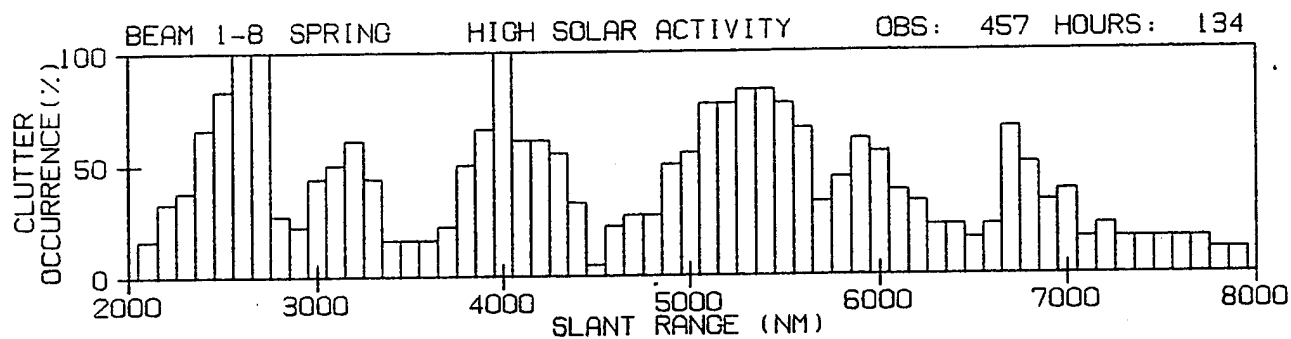
Figure 9. Frequency of occurrence with slant range of clutter for fall season for high and low solar activity periods for beam 3-5.

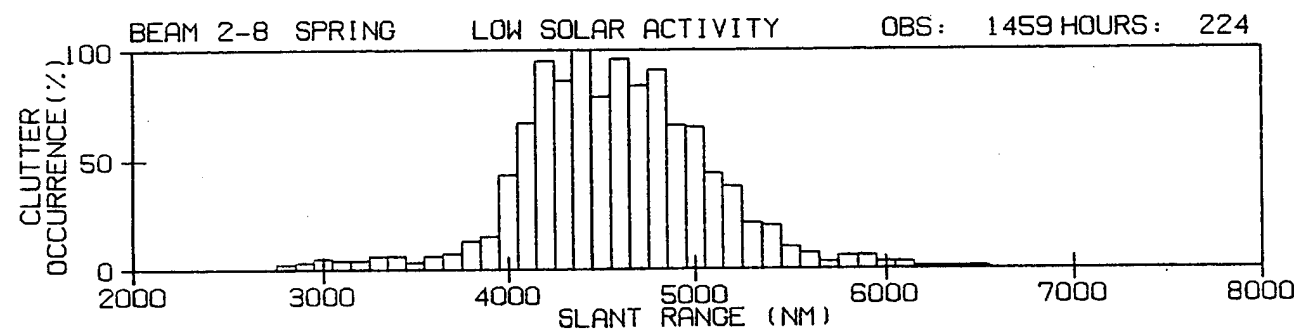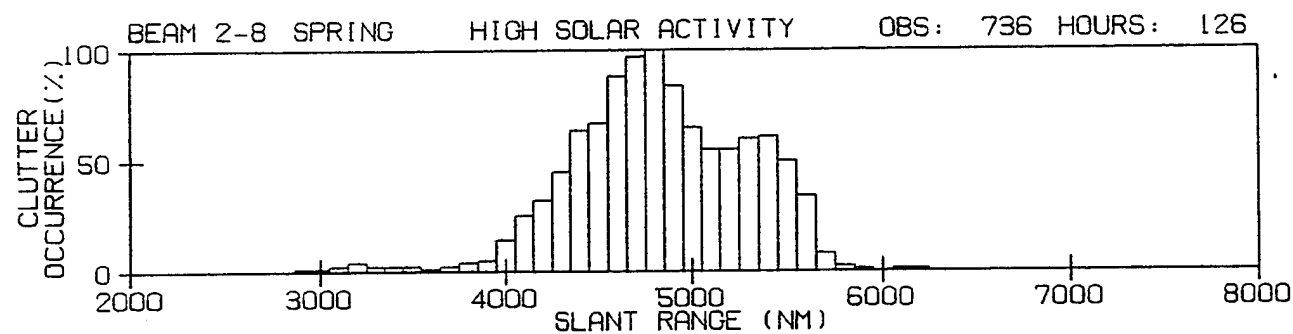frequency of occurrence histograms shows that during a high solar activity period (upper section) the major clutter was in the range of 4600-5100 nmi range, whereas at low solar activity the corresponding clutter covered a range of 4400-4900 nmi. Thus clutter at high solar activity was 200 nmi farther away from the radar than that at low solar activity. For the fall season there are not enough data for other beams for such comparisons.

For the winter season these data are available for beams 1-8, 2-4, 2-8, and 3-5 (no data for beam 1-6 were available for comparison). These are presented in Figure 10. For beam 1-8 at high solar activity there are at least two clutter regions; one around 3200-3600 nmi range (midlatitude clutter) and the other at 4800-5500 nmi range (northern anomaly), and possibly a third one at 4000-4400 nmi range (midlatitude clutter). The clutter range for high solar activity at 4800-5500 nmi shortens to 4600-5400 nmi at low solar activity. For beam 2-4 the clutter range of 4800-5200 nmi at high solar activity spreads as the distribution moves down to 4400-5400 nmi. A similar change is
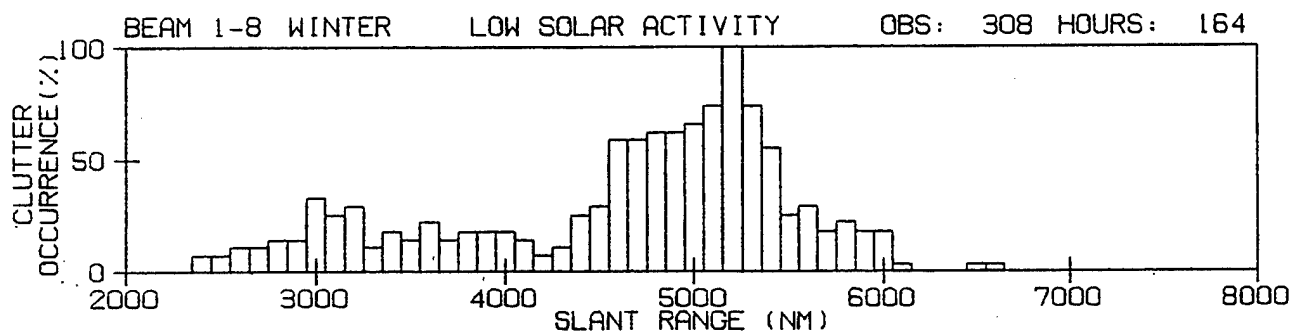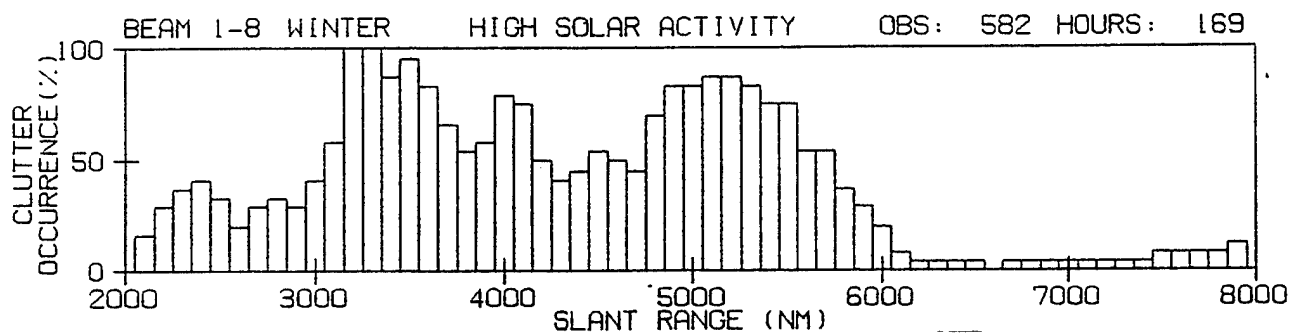
10 A. Frequency of occurrence with slant range of clutter for winter season for high and low solar activity periods for beam 1-8.
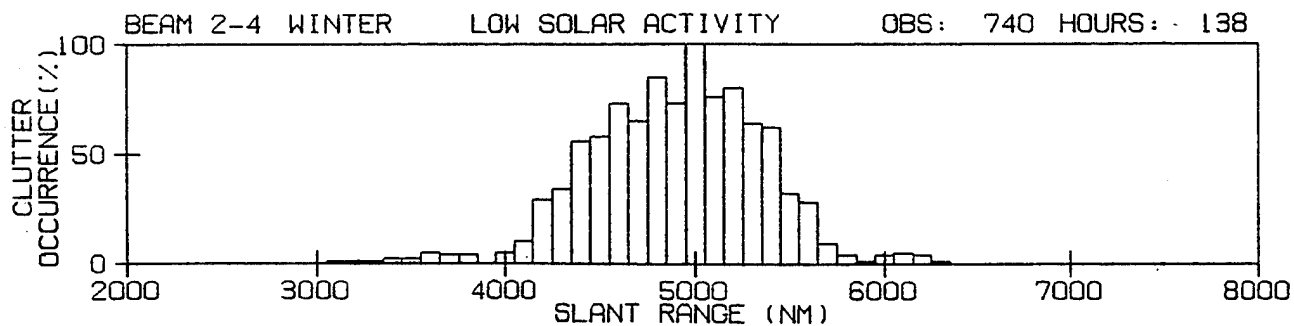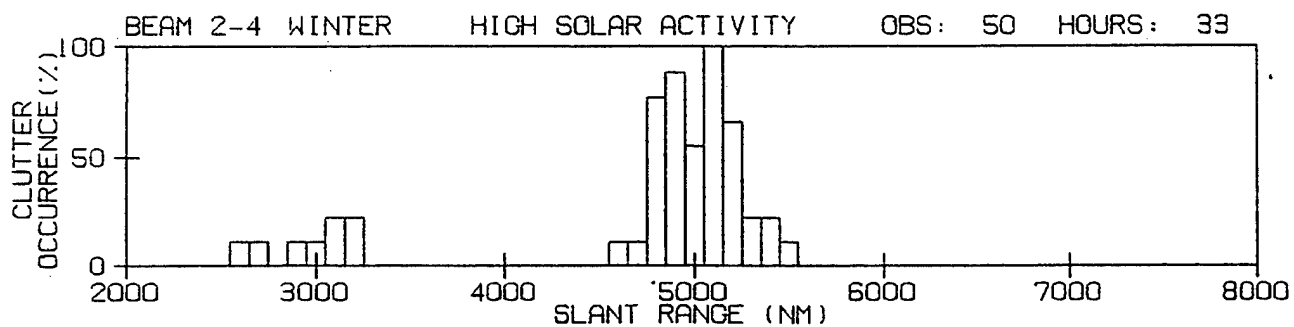
10 B. Frequency of occurrence with slant range of clutter for winter season for high and low solar activity periods for beam 2-4.

36
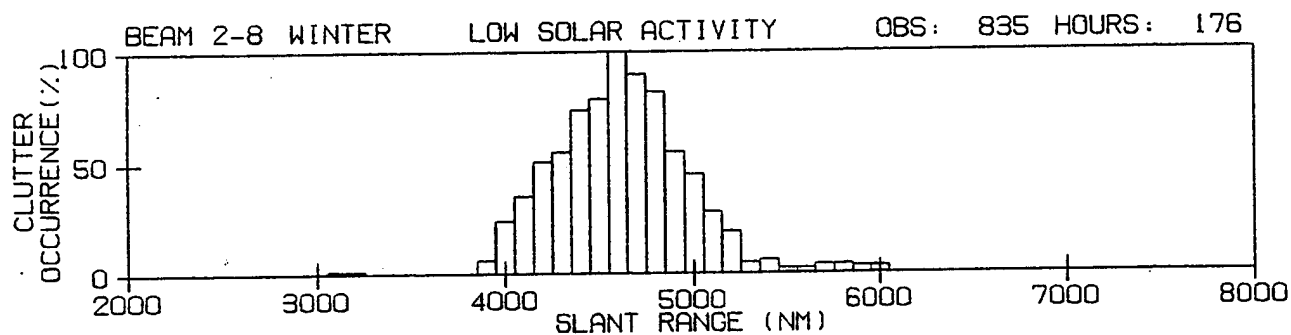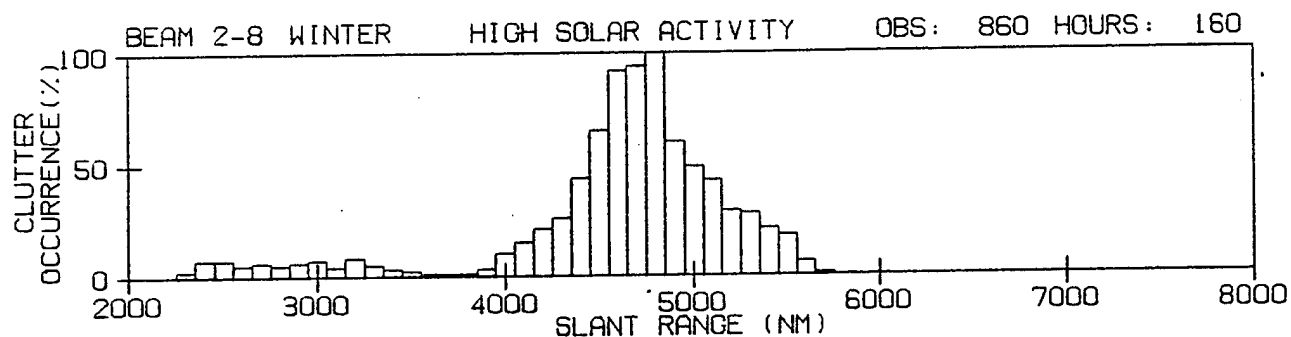
10 C. Frequency of occurrence with slant range of clutter for winter season
for high and low solar activity periods for beam 2-8.

10 D. Frequency of occurrence with slant range of clutter for winter season
for high and low solar activity periods for beam 3-5.

seen for beam 2-8 with the clutter range moving from 4500-4900 nmi for a high solar activity period to 4200-4900 nmi for a low solar activity period. Also, in beam 3-8 the clutter range of 4500-5200 nmi in a high solar activity period moves to 4400-4800 nmi in a low solar activity period. Thus in winter, a consistent shortening of the clutter range is seen from periods of higher to lower solar activity.

In Figure 11 for the spring season the data for relative frequency of clutter occurrence vs range are shown for beams 1-8, 2-8, and 3-5 (there are no data for beams 1-6 and 2-4 for comparison). For beam 1-8 the distribution shows multiple peaks (midlatitude clutter and northern anomaly) for occurrence. The figure shows that for beam 1-8 the range of 5000-5600 nmi at high solar activity moves to 4600-5800 nmi during the low solar activity period. For beams 2-8 and 3-5, ranges of 4400-5400 and 4400-5100 nmi at high solar activity move to lower values of 4100-5000 and 4000-4900 nmi respectively at low solar activity.

For the summer season the data are available for all the beams: 1-6, 1-8, 2-4, 2-8, and 3-5. These are presented in Figure 12. For beam 1-6 the major peak has the ranges 5000-5600 and 5300-5600 nmi at high and low solar activity periods respectively, showing no significant difference. For beam 1-8 the major peak is very different, lying at a range of 6600-7000 nmi (the southern anomaly is significantly different than in other beams) for both high and low solar activity periods. Again, beam 2-4 shows a slightly opposite tendency, the clutter range being 4100-5000 nmi at high solar activity and 4400-5300 nmi at low solar activity. Beam 2-8 shows no significant change in range, clutter being at 3900-4800 nmi at high and 3800-4400 nmi at low solar activity. Similarly, beam 3-5 shows no significant change in range, 4400-4800 nmi at high and 4200-4800 nmi at low solar activity. A few points to be noted are :1) the movement of the clutter range with respect to high and low solar periods is determined from the clutter distribution histograms; the ranges quoted are at 50 percent level, 2) the peaks seen for beams 1-8 (6600-7000), 2-8 (4200-4800 nmi) are different than those seen around 5000 nmi range, suggesting different sources of clutter for these three ranges. Thus in summer no clear shortening of clutter range is seen with change in solar activity. In all other seasons the range of clutter occurring around 5000 nmi during high solar activity is lowered by 200-400 nmi during periods of low solar activity. Later it is shown that the lowering of clutter range seen is caused by changes in the ray geometry for the corresponding periods. No systematic change in the frequency range of the clutter with season was observed.

BEAM 1-8 SPRING   HIGH SOLAR ACTIVITY   OBS: 457 HOURS: 134

CLUTTER OCCURRENCE (%)

SLANT RANGE (NM)

BEAM 1-8 SPRING   LOW SOLAR ACTIVITY   OBS: 819 HOURS: 231
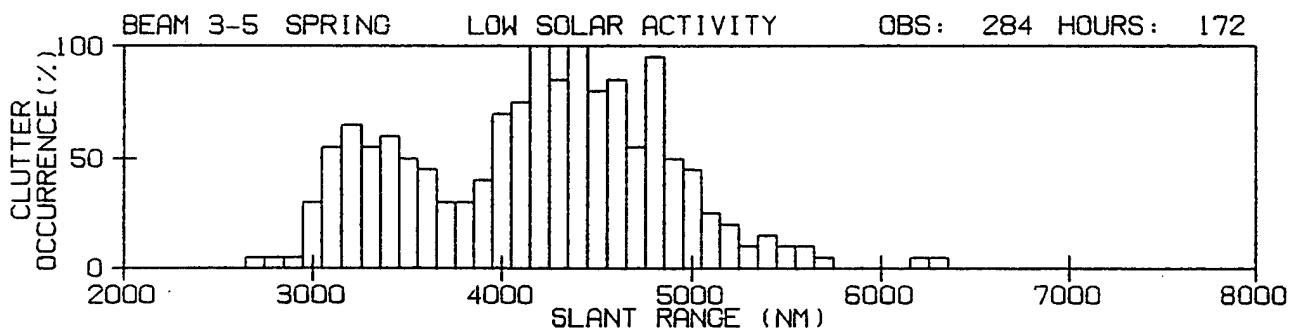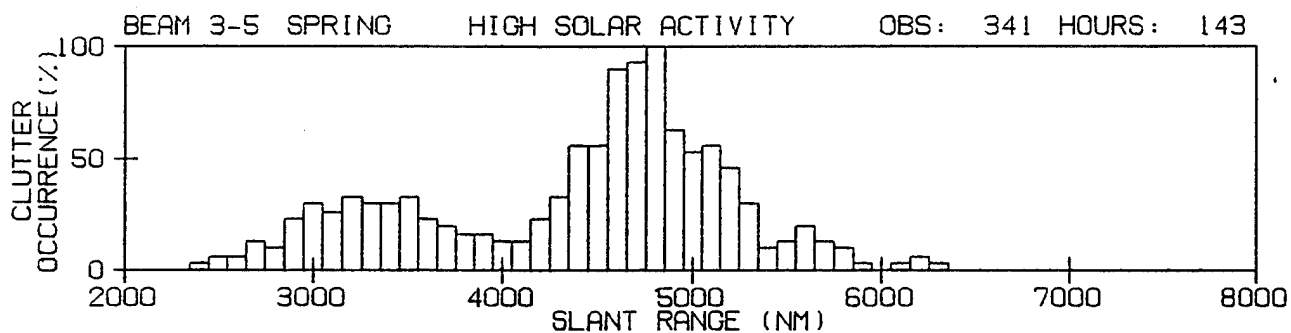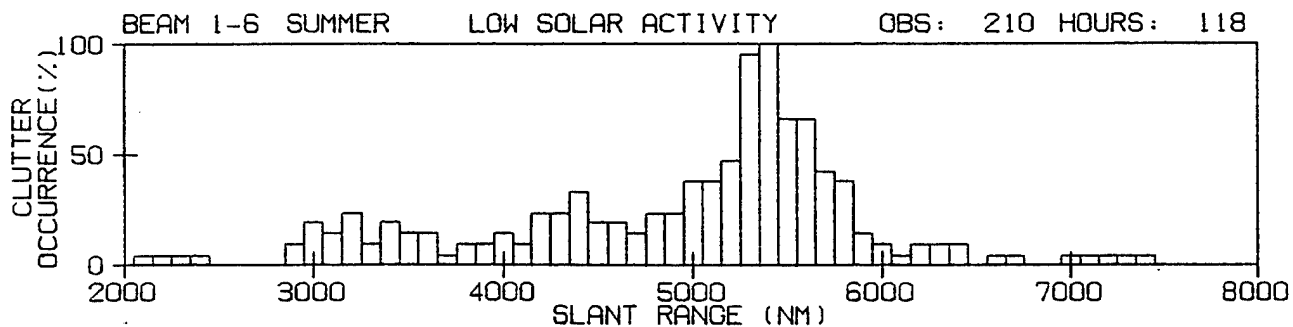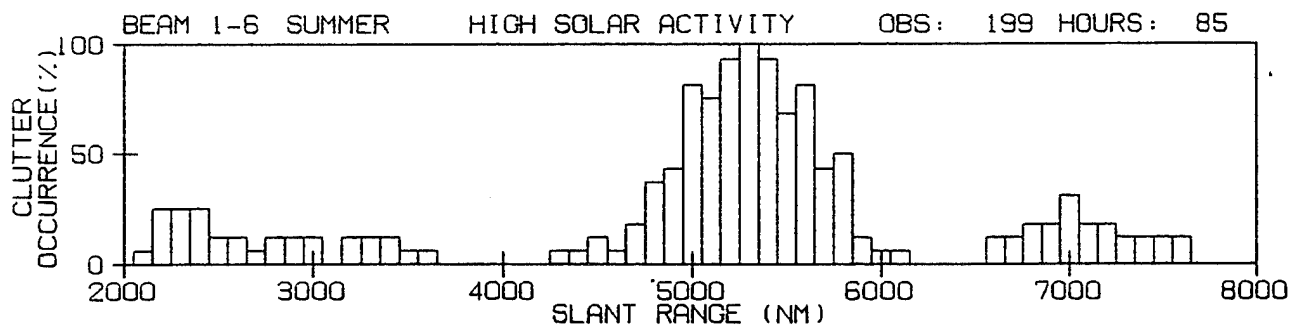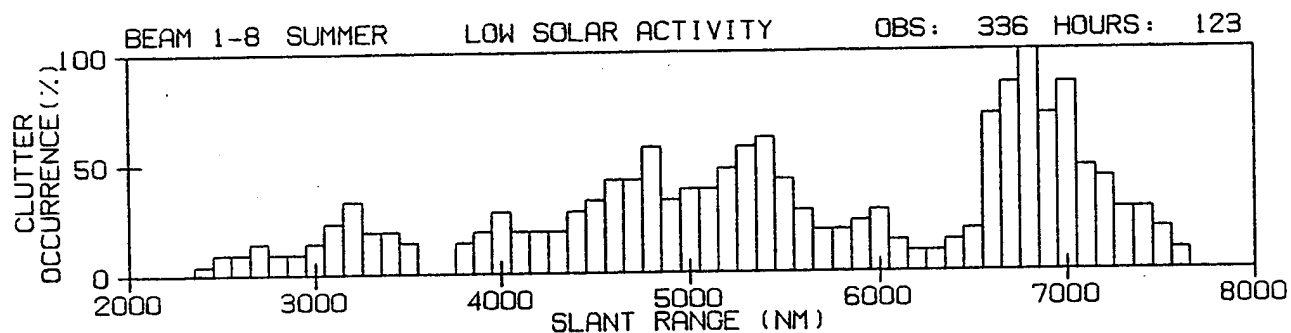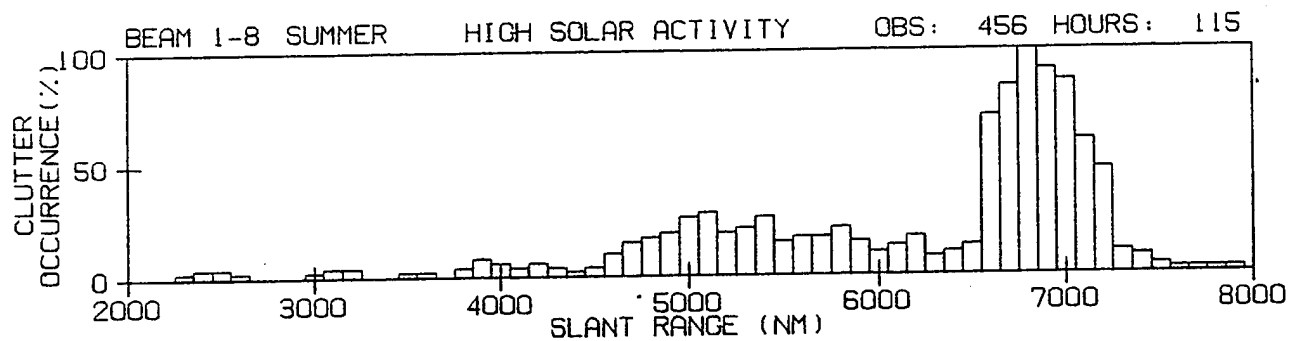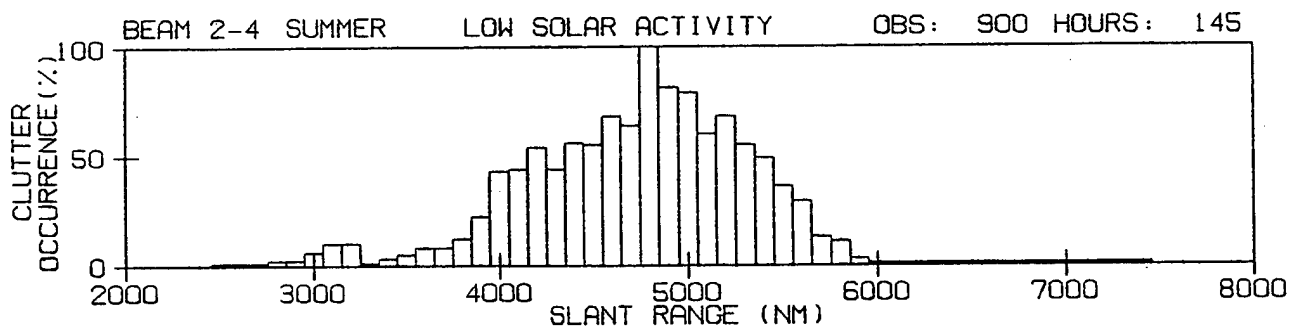
CLUTTER OCCURRENCE (%)

SLANT RANGE (NM)

11 A. Frequency of occurrence with slant range of clutter for spring season for high and low solar activity periods for beam 1-8.

BEAM 2-8 SPRING   HIGH SOLAR ACTIVITY   OBS: 736 HOURS: 126

CLUTTER OCCURRENCE (%)

SLANT RANGE (NM)

BEAM 2-8 SPRING   LOW SOLAR ACTIVITY   OBS: 1459 HOURS: 224

CLUTTER OCCURRENCE (%)

SLANT RANGE (NM)

11 B. Frequency of occurrence with slant range of clutter for spring season for high and low solar activity periods for beam 2-8.

11 C. Frequency of occurrence with slant range of clutter for spring season
for high and low solar activity periods for beam 3-5.

12 A. Frequency of occurrence with slant range of clutter for summer season
for high and low solar activity periods for beam 1-6.

40

12 B. Frequency of occurrence with slant range of clutter for summer season
for high and low solar activity periods for beam 1-8.
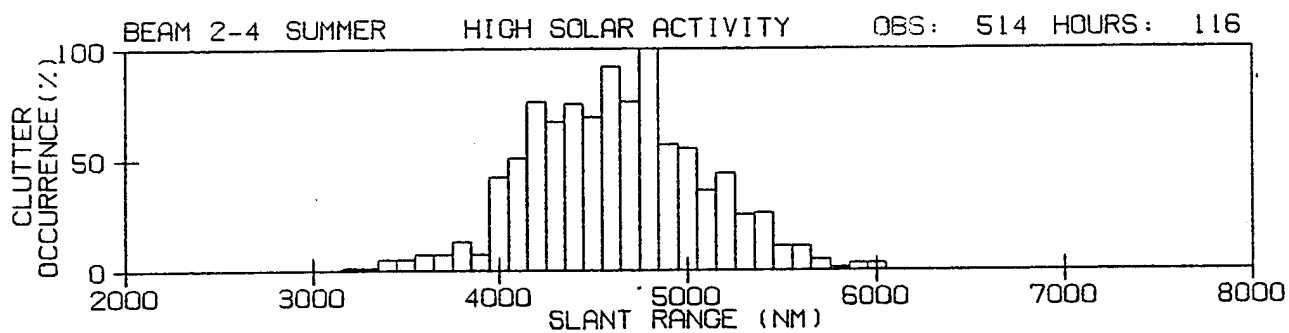
12 C. Frequency of occurrence with slant range of clutter for summer season
for high and low solar activity periods for beam 2-4.
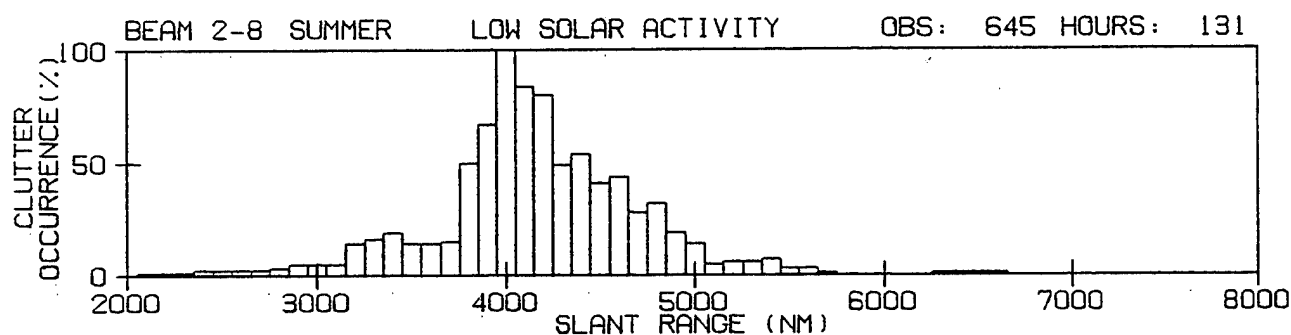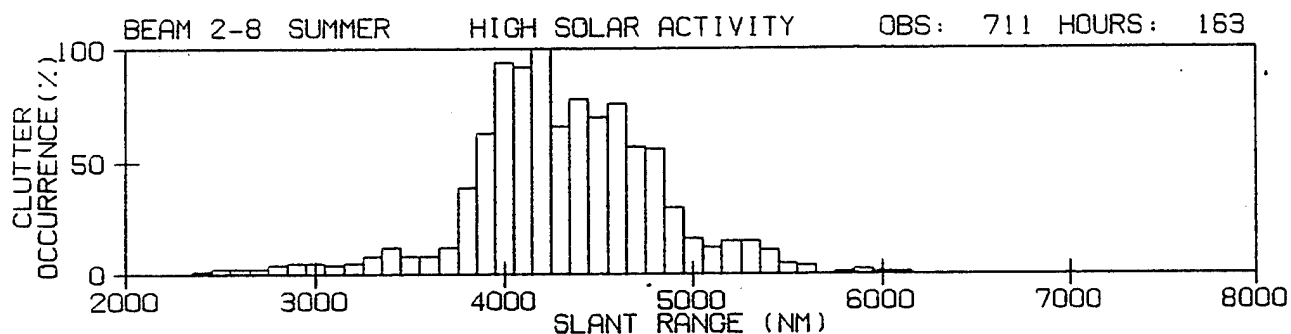
12 D. Frequency of occurrence with slant range of clutter for summer season for high and low solar activity periods for beam 2-8.
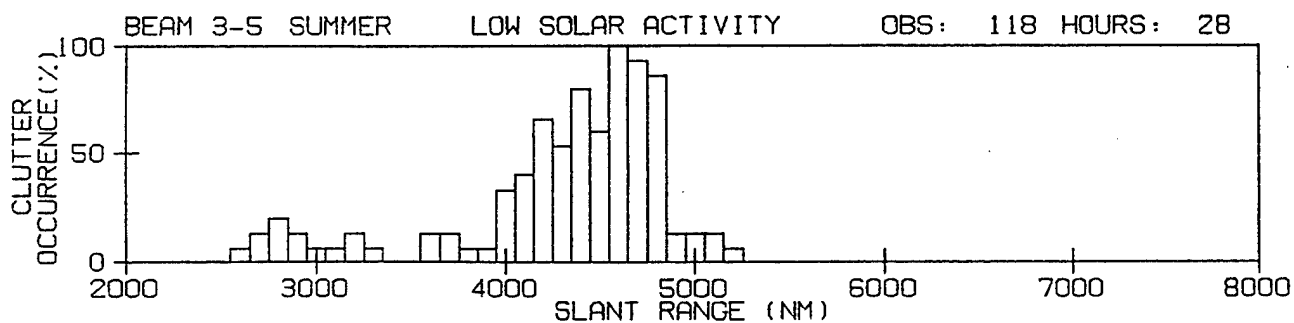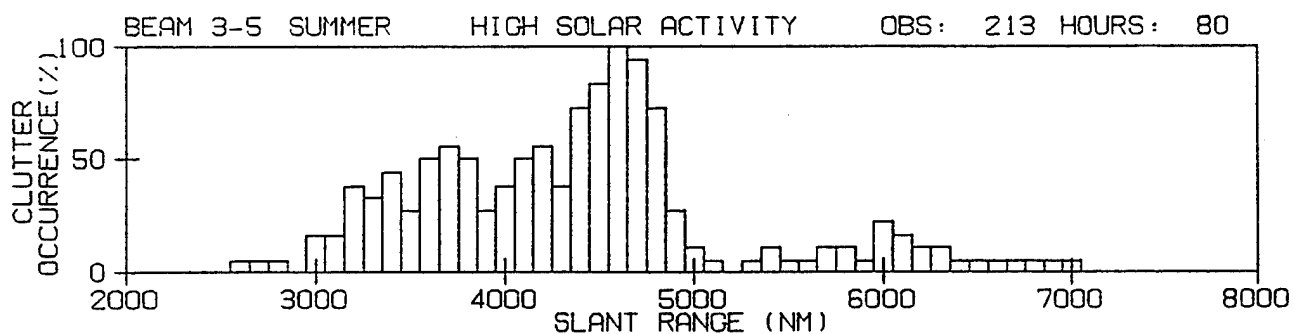
12 E. Frequency of occurrence with slant range of clutter for summer season for high and low solar activity periods for beam 3-5.

42

To determine the effect of magnetic activity on the clutter occurrence, all the data were sorted in two groups of very high and very low levels of magnetic activity. The groups consisted of the quiet(Q) and disturbed (D) conditions listed for each month by the World Data center, Boulder, Colorado, USA. The comparison of these two data sets for each beam (Table 2) for clutter range, and frequency of occurrence did not show any significant differences. Therefore from this data set, it is concluded that the observed clutter is independent of the level of magnetic activity, to be expected for the equatorial region.

Typical diurnal behavior of clutter for beams 3-5, 2-8, and 1-8 for the winter season in 1991-92 for a high solar activity period (sunspot number SSN=130) is presented in the following figures. Figure 13 shows typical hourly BSIs for beam 3-5, looking at an azimuth of 170.25° T, essentially along a constant local time. The first BSI at 1959 UT shows only ground returns from the first, second, and third hop reflection modes. At 2056 UT additional reflections are seen at around the slant range of 5000 nmi for the frequency bands of 10.0-15.4 and 24.6-28.0 MHz. A wide horizontal strip at a slant range of 4800 nmi. running practically the entire frequency band is seen for next three hours (until 2337 UT). At 0103 UT a wide horizontal strip is seen around 5000 nmi over a frequency band of 11.8-19.0 MHz. At 0213 UT the frequency band covers a range of 19.0-24.4 MHz. No typical data are available for 0300 UT. In the last hourly sample for 0413 UT reflections requiring as many as five hops are seen. The figure shows that equatorial clutter starts around sunset and continues up to midnight.

Figure 14 shows a time sequence of BSIs for beam 2-8 looking at azimuth of 132.75° T. Because beam 2-8 looks more easterly than beam 3-5, the clutter starts an hour earlier (1900 UT vs 2000 UT). The equatorial clutter is strong and prominent in this beam as compared to that in the former. The clutter is clearly seen at 0410 UT, the last typical BSI available for this beam. One of the possible reasons for strong clutter in this beam is that the reflections for beam 2-8 are mostly over the ocean surface in contrast to those for beam 3-5 over the land terrain.

Figure 15 shows the typical hourly BSIs for beam 1-8 with an azimuth of 72.75° T looking practically due east of the transmitter site, covering a time zone 9 hours wide. Here the clutter occurs at 2100 UT and continues all the way through 0700 UT, the last typical BSI available for this beam. In contrast to beams 3-5 and 2-8, the clutter is fragmented and occurs at multiple locations. The cause for such different behavior is not understood.

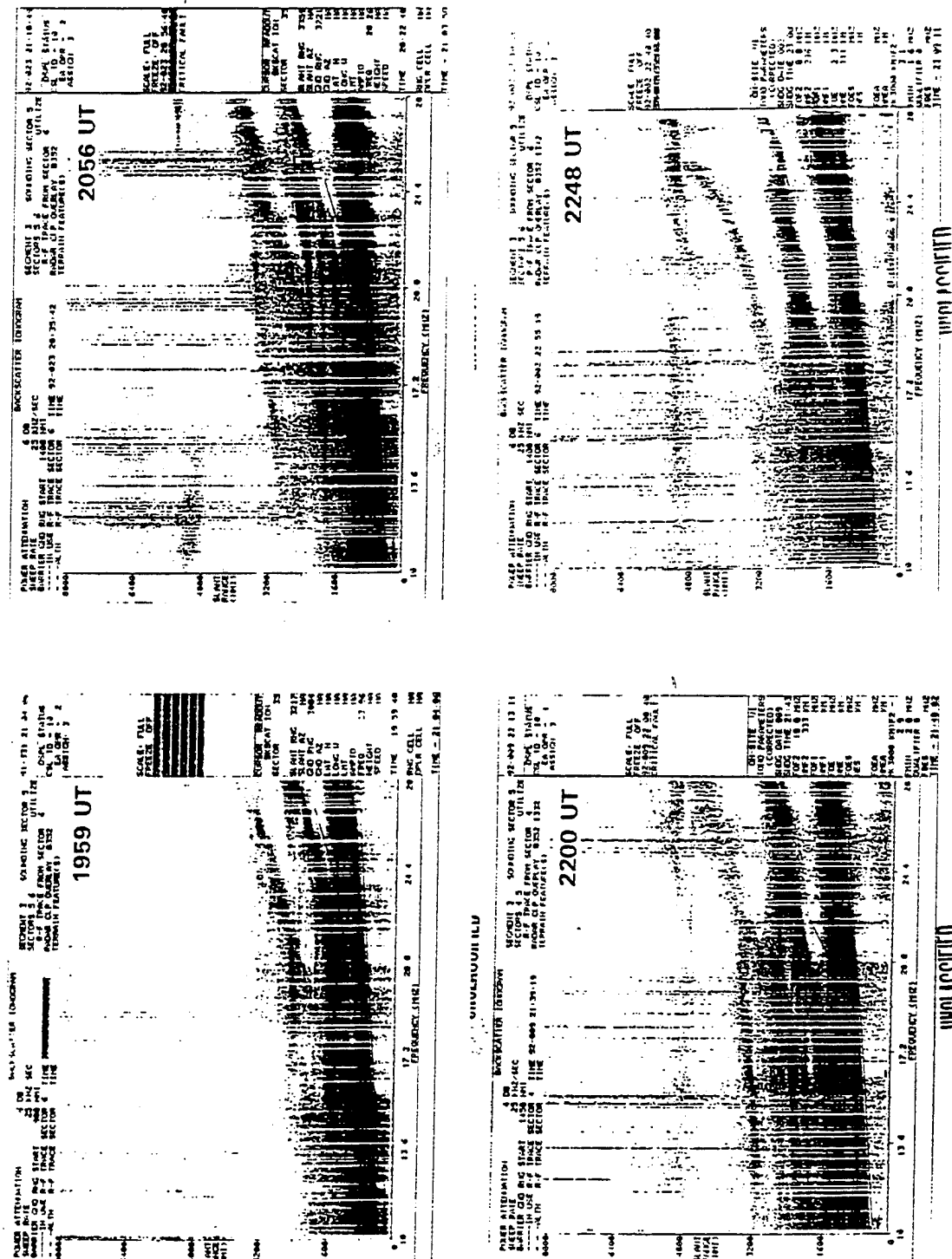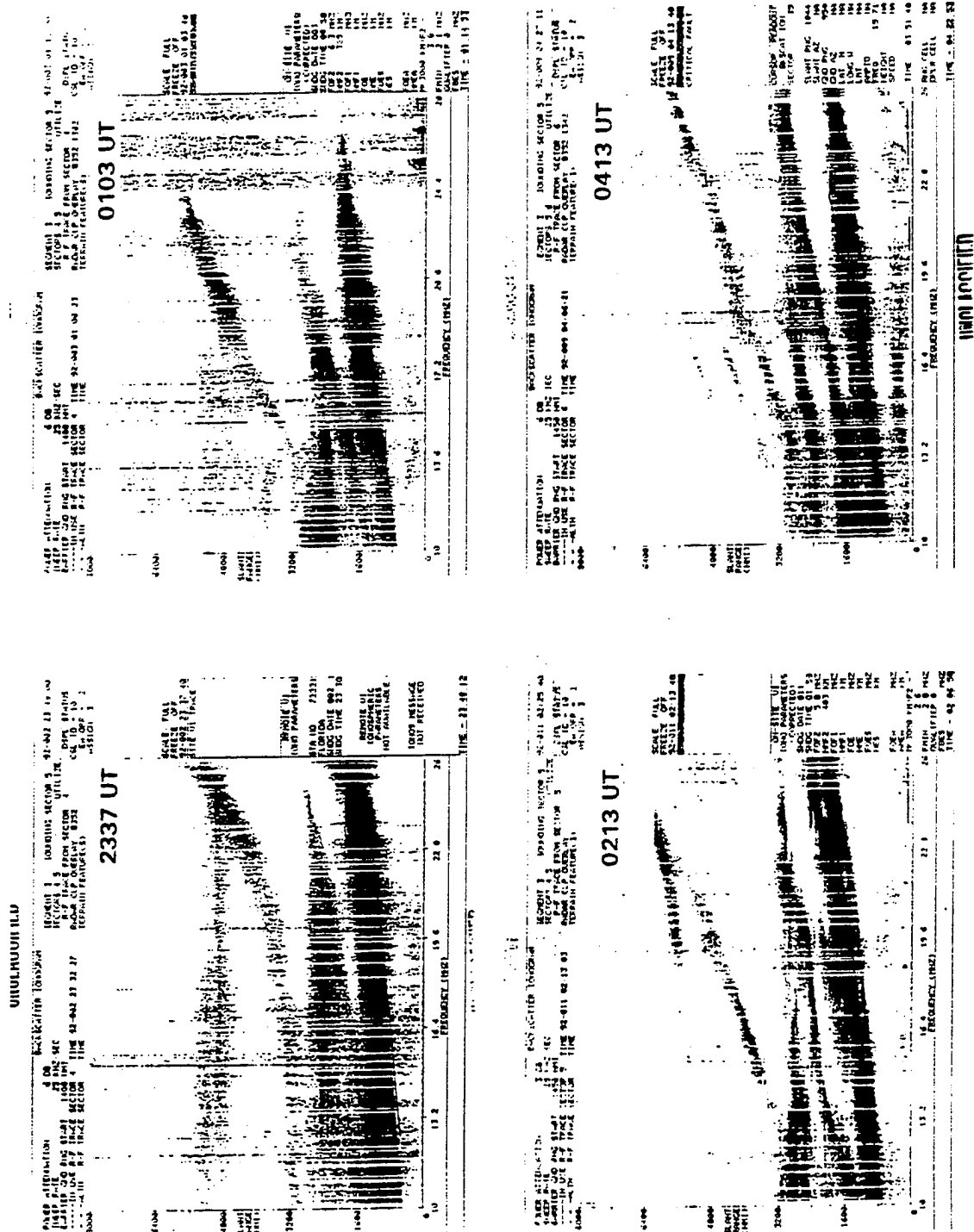# BACKSCATTER IONOGRAMS   WINTER 91-92   SEGMENT 3   SECTOR 5

Figure 13. Time sequence for typical behavior of equatorial clutter in beam 3-5 for the winter 1991-92, the period of high solar activity (SSN=130).

44

BACKSCATTER IONOGRAMS WINTER 91-92 SEGMENT 3 SECTOR 5

Figure 13. Time sequence for typical behavior of equatorial clutter in beam 3-5 for the winter 1991-92, the period of high solar activity (SSN=130) ,-continued.

45

Figure 14. Time sequence for typical behavior of equatorial clutter in beam 2-8 for the winter 1991-92, the period of high solar activity (SSN=130).

BACKSCATTER IONOGRAMS WINTER 91-92 SEGMENT 2 SECTOR 8

Figure 14. Time sequence for typical behavior of equatorial clutter in beam 2-8 for the winter 1991-92, the period of high solar activity (SSN=130) , -continued.

47

BACKSCATTER IONOGRAMS WINTER 91-92 SEGMENT 2 SECTOR 8

Figure 14. Time sequence for typical behavior of equatorial clutter in beam 2-8 for the winter 1991-92, the period of high solar activity (SSN=130) , -continued.

BACKSCATTER IONOGRAMS WINTER 91-92 SEGMENT 1 SECTOR 8

Figure 15. Time sequence for typical behavior of equatorial clutter in beam 1-8 for the winter 1991-92, the period of high solar activity (SSN=130).

49

BACKSCATTER IONOGRAMS WINTER 91-92 SEGMENT 1 SECTOR 8

Figure 15. Time sequence for typical behavior of equatorial clutter in beam 1-8 for the winter 1991-92, the period of high solar activity (SSN = 130), -continued.
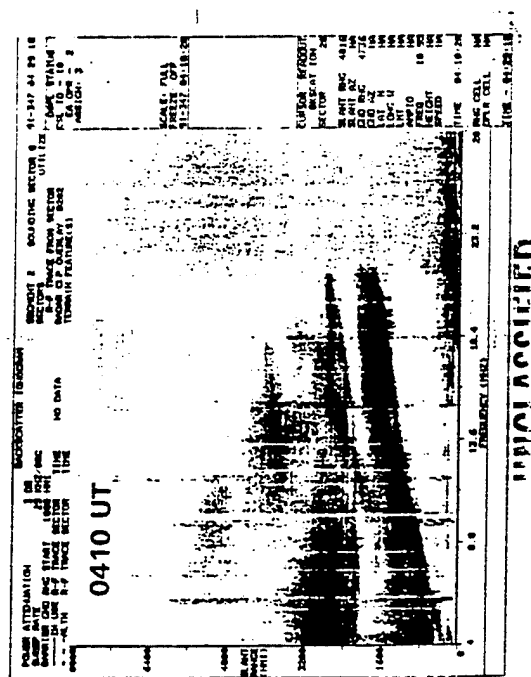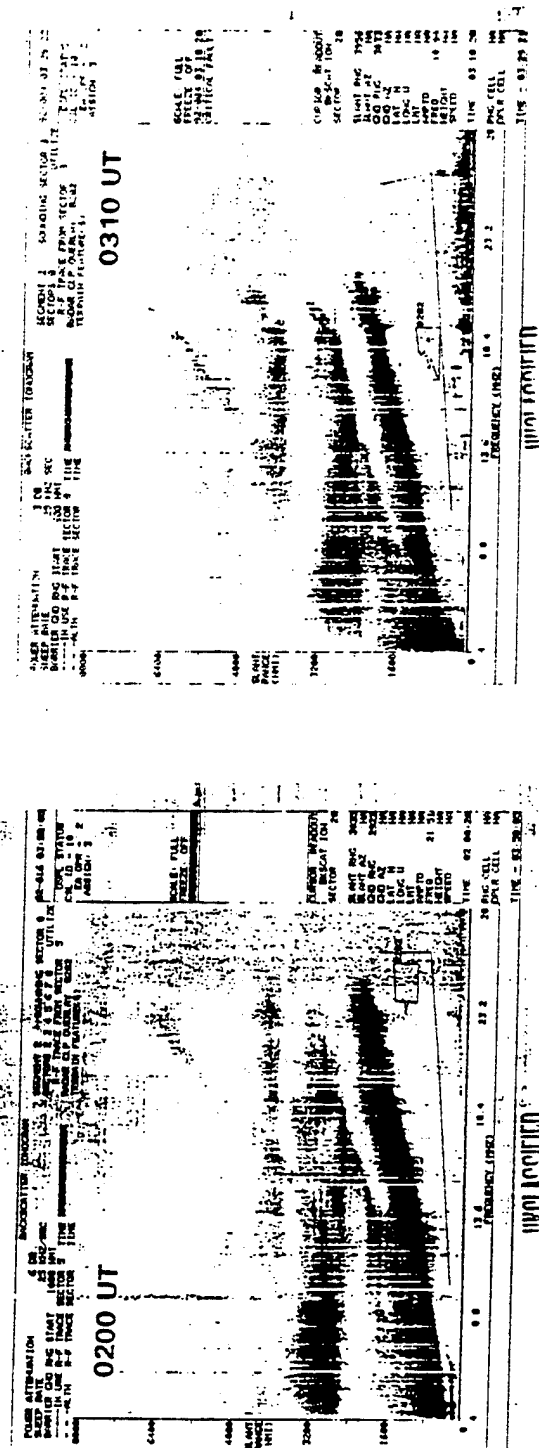
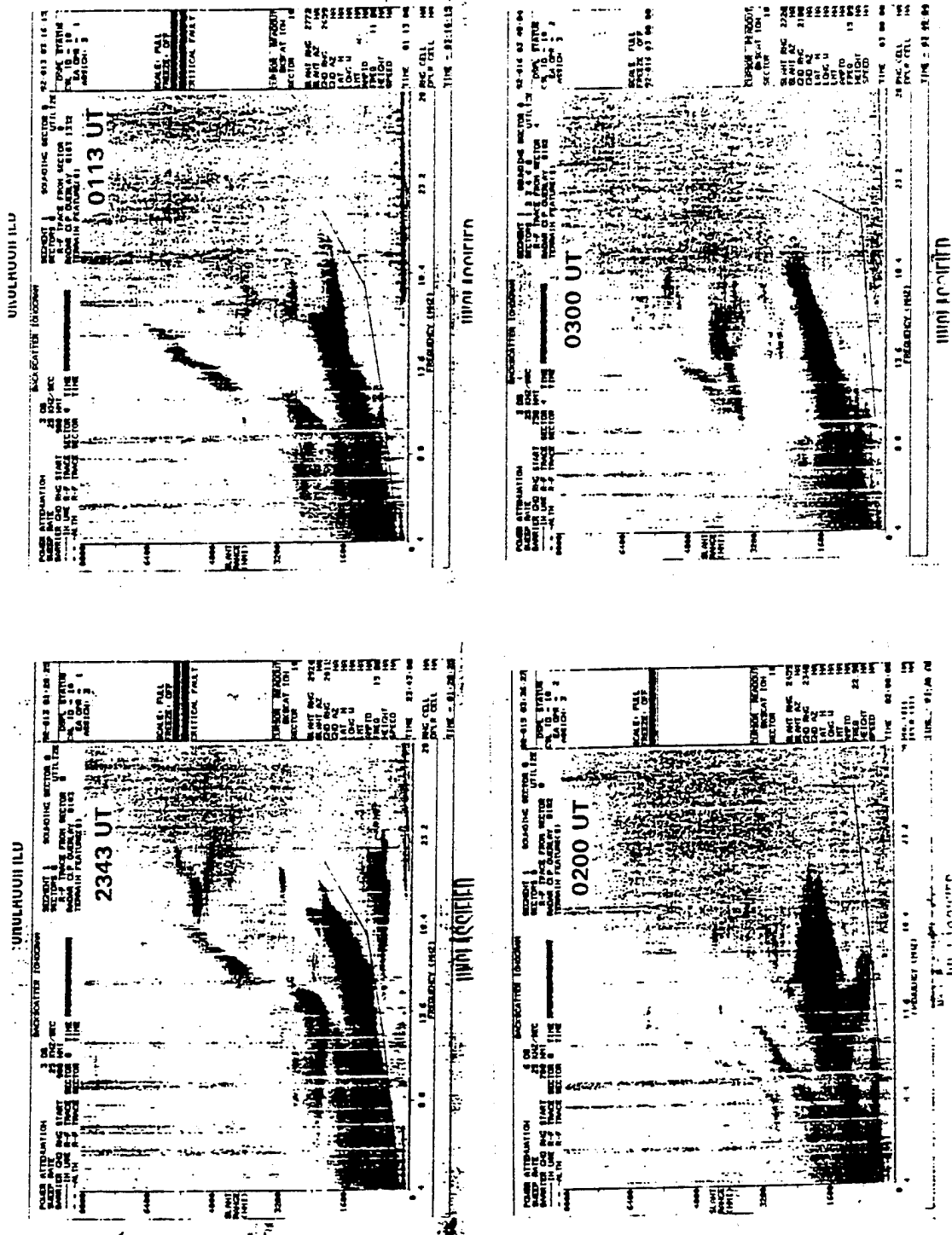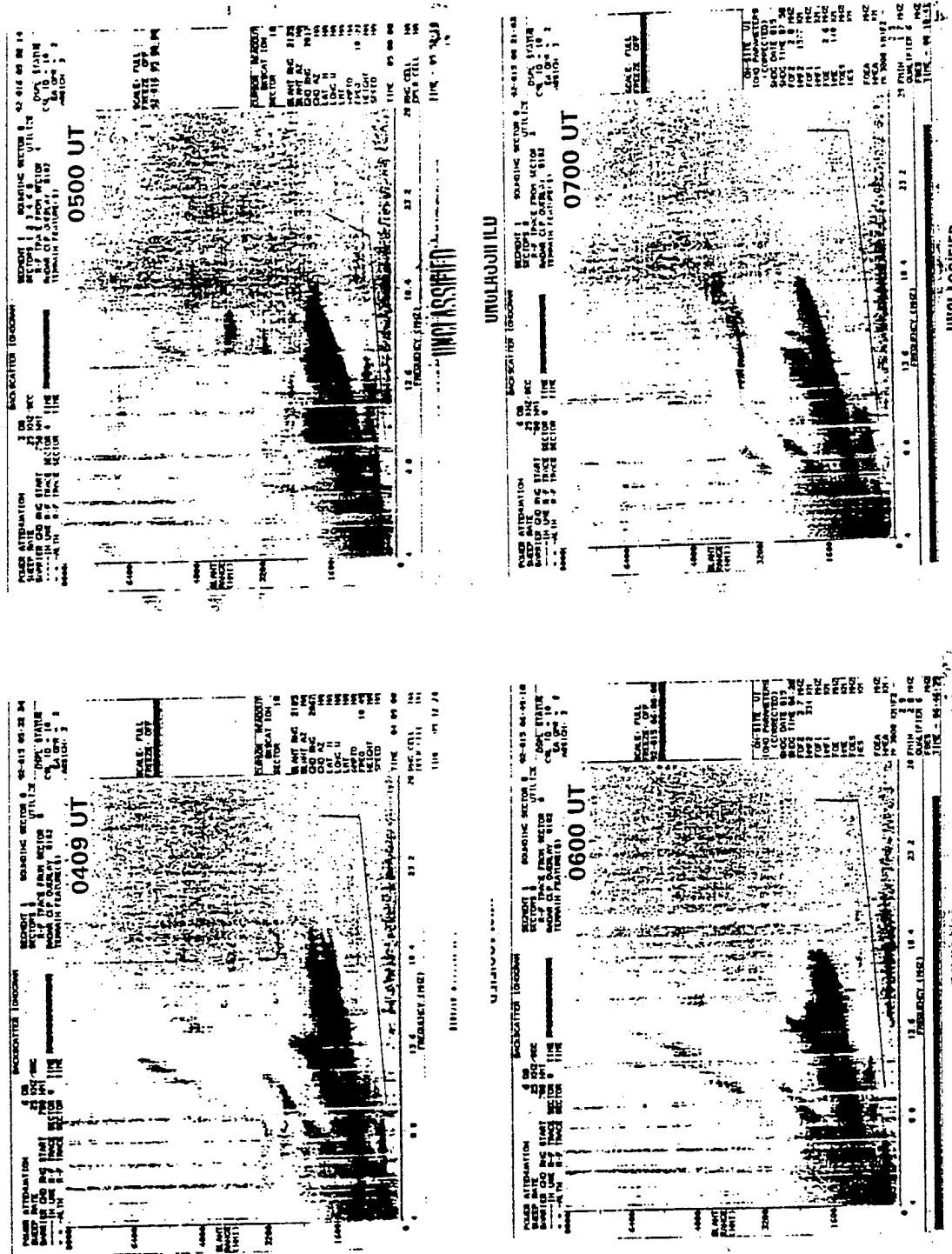# BACKSCATTER IONOGRAMS WINTER 91-92 SEGMENT 1 SECTOR 8

Figure 15. Time sequence for typical behavior of equatorial clutter in beam 1-8 for the winter 1991-92, the period of high solar activity (SSN=130), -continued

51

5. SYNTHETIC BACKSCATTER IONOGRAMS

Generating synthetic backscatter ionograms requires several steps. First one selects an ionospheric model and determines the electron density distribution with respect to altitude along the desired raypath (azimuth for which the backscatter ionogram is sought). Then one uses a raytrace program to determine the range (distance from the transmitter) of the ground reflection points along the selected path. For the given ionosphere this range is a function of the elevation angle and the operating frequency. The signatures of the ground reflection points in terms of raypath distance, that is, slant range (time delay between the transmitted and the received signals) versus frequency, form the backscatter ionogram.

For the construction of the long range backscatter ionograms the Parameterized Ionospheric Model[1] (PIM) developed by Anderson (Daniell et al., 1994) at Phillips Laboratory is used. For raytracing, the program by Jones and Stephenson[2] (1975) is used. The PIM model is appropriate for the equatorial clutter study as it includes features such as $E \times B$ drift and neutral winds that are absent in other climatological models such as IONCAP[3]. Although the peak f_oF_2 values are very similar in PIM and IONCAP models, the altitude dependence of the electron density profiles is modified in PIM as compared to that in IONCAP. As an example, Figure 16 shows two f_oF_2 contours, one from IONCAP and the other from the PIM model for high solar activity level (SSN=130) for a winter day for the ECRS looking at an azimuth 170° (beam 3-5). Note that the general structure of the contours is very similar. The altitude of the maximum density is marked on both the IONCAP on the PIM contour maps. Note that distance of the magnetic dip equator is about 6600 km from the radar. At the equator the maximum in the PIM model is at an altitude of 510 km, 62 km above that of the IONCAP model. This difference reduces with increasing range from the dip equator. Figure 17 shows that for the same winter day, with SSN=75, the PIM maximum of f_oF_2 is at 470 km, 98 km above that of IONCAP. In the PIM model the altitude difference for peak f_oF_2 between high and low sunspot activity is 40 km. Raytraces in these figures show that the radar wave propagation is basically contained in the bottom portion of the ionosphere. Thus the raytrace computations yield slightly longer ranges for the PIM model than those for the IONCAP model because the entire layer is consistently higher in the PIM model than those in the IONCAP model. Similarly for a given frequency ratio ($f_{operating}/f_oF_2$), the higher altitudes for higher sunspot

COMPARISON OF IONOSPHERIC MODELS IONCAP AND PIM 1-06
ORIGIN 44.80°N 292°E   AZIMUTH 170.3°
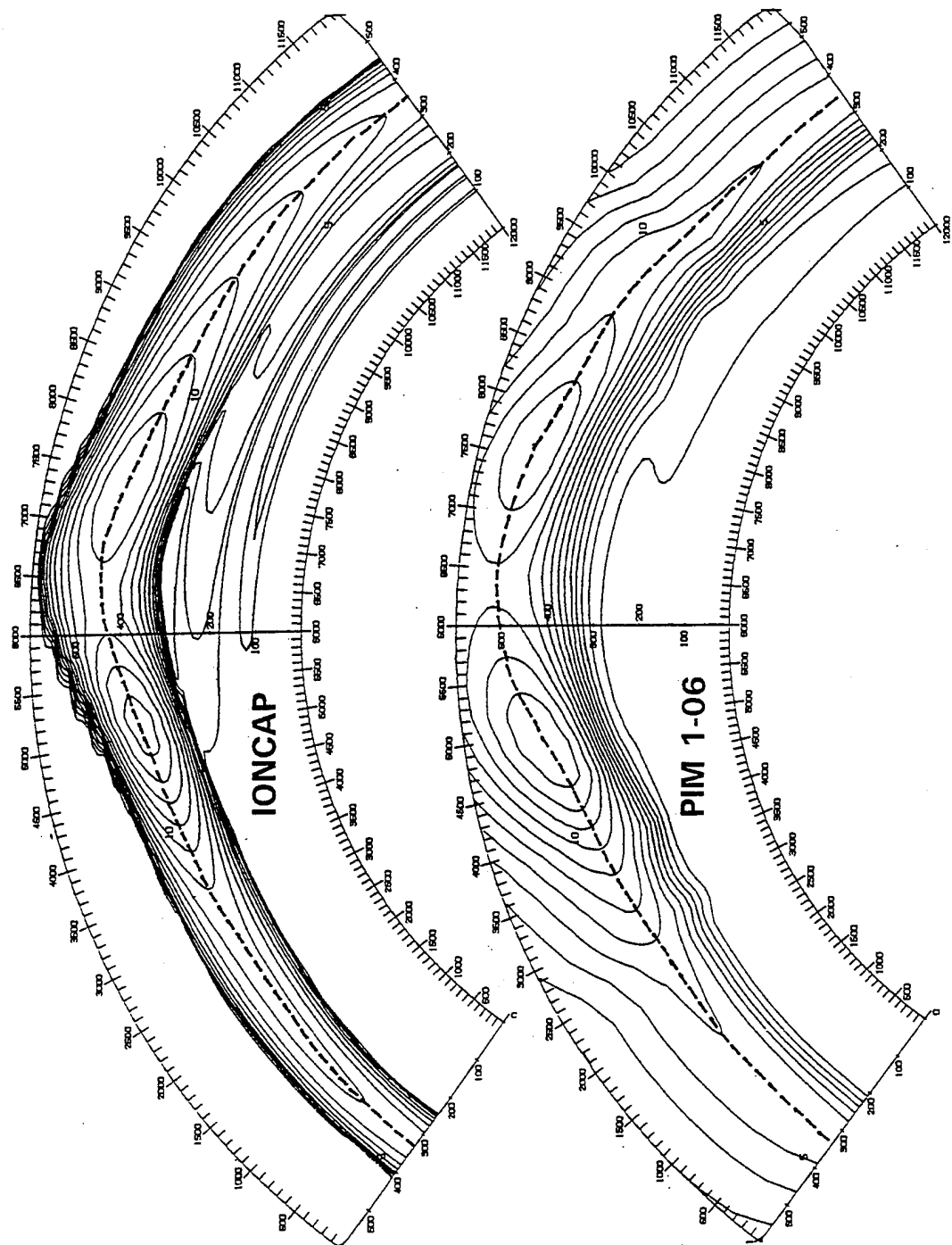DECEMBER   2300 UT   SSN = 130   KP = 2   Q = 2

IONCAP

PIM 1-06

Figure 16. f_oF_2 contours from the IONCAP and PIM models for high solar activity (SSN=130) for day 354 for 2300 UT. Note the difference in peak altitudes near the magnetic equator.

COMPARISON OF IONOSPHERIC MODELS IONCAP AND PIM 1-06
ORIGIN 44.80°N 292°E   AZIMUTH 170.3°
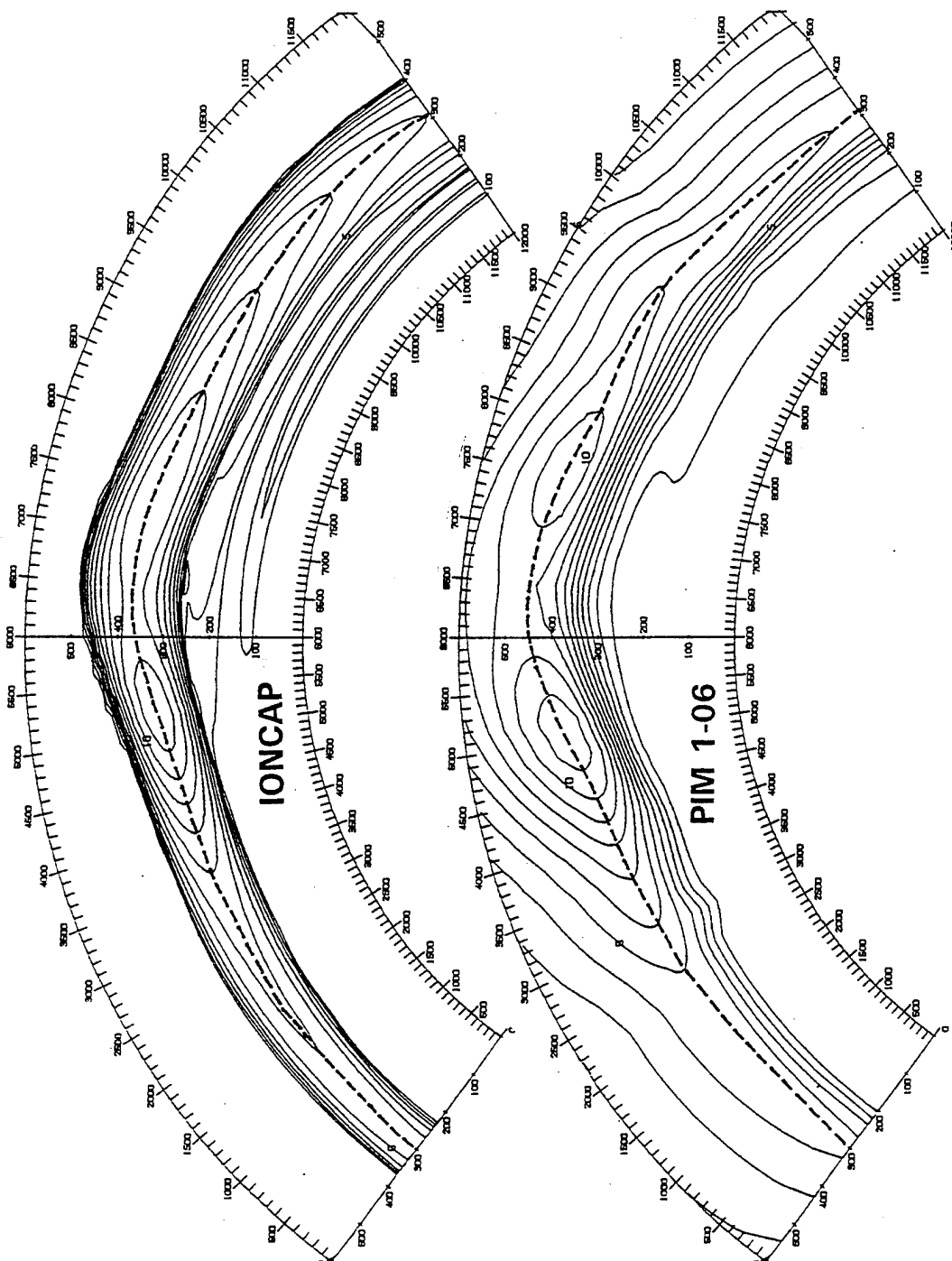DECEMBER   2300 UT   SSN = 75   KP = 2   Q = 2

IONCAP

PIM 1-06

Figure 17. f_oF_2 contours from the IONCAP and PIM models for low solar activity (SSN=75) for (winter) day 354 for 2300 UT. Note the difference in peak altitudes near the magnetic equator.

number/activity result in longer ranges than those for low sunspot number/activity. This is why the equatorial clutter ranges are longer for the high sunspot period of 1991-1992 than those for low sunspot activity of 1992-1993 (see Figures 9-12).

Figure 18 shows the time dependence of the altitude of peak of f_oF_2 at the dip equator for beams 3-5, 2-8, and 1-8 for high and low solar activity (SSN=130 and 75 respectively) for a winter day. As the beams look from south to east (170°, 132°, 72°) the time of the maximum is from 0100, 2300, and 1900 UT respectively. The occurrence frequency listed in Table 3, and the time sequence of clutter behavior seen in Figures 13-15, is consistent with this pattern. In Figure 18 the altitudes are consistently higher during a high solar activity period than those for the low solar activity period. Thus the clutter ranges would be consistently longer during a high solar activity period than those at the low solar activity periods (see Figures 7 to 12).

Figure 19 presents raytraces for beam 2-8, for a winter day, for high solar activity (SSN=130) for operating frequencies of 14, 16, and 18 MHz. The common features of these raytraces are 1) the ionosphere closer to the radar within the first hop range provides the main control for the wave propagation, 2) the wave propagation is basically restricted to the bottom portion of the F_2 layer, and 3) the equatorial dome geometry of the f_oF_2 distribution favors a chordal mode of reflection. Figure 20, presenting raytraces for low solar activity (SSN=75) supports the same conclusions. For a direct comparison of the change in range with solar activity, it is necessary to compare raytraces with equal ratios of $f_oF_2/f_{operational}$ instead of equal operational frequencies.

From the raytraces shown in Figures 19 and 20, synthetic backscatter ionograms are generated and are shown in Figure 21. The upper panel is for high solar activity and the lower panel is for low solar activity. The highest frequency for the top BSI is 24 MHz, whereas for the bottom BSI, it decreases to 19 MHz due to lower f_oF_2 at low solar activity (see f_oF_2 contours in Figures 19 and 20). Note the first three ground hop signatures at the bottom are followed by heavy, nearly horizontal traces around 8000 km range. These horizontal traces indicate chordal mode due to reflection from the southern side of the equatorial dome, and the horizontal trace at low solar activity has a shorter range than the trace at high solar activity.

To demonstrate the difference in raypaths for beam 1-8, compared to beams 3-5 and 2-8, the raytraces for 12 and 14 MHz are shown in Figure 22. For beam 1-8 the equatorial dome is far away,
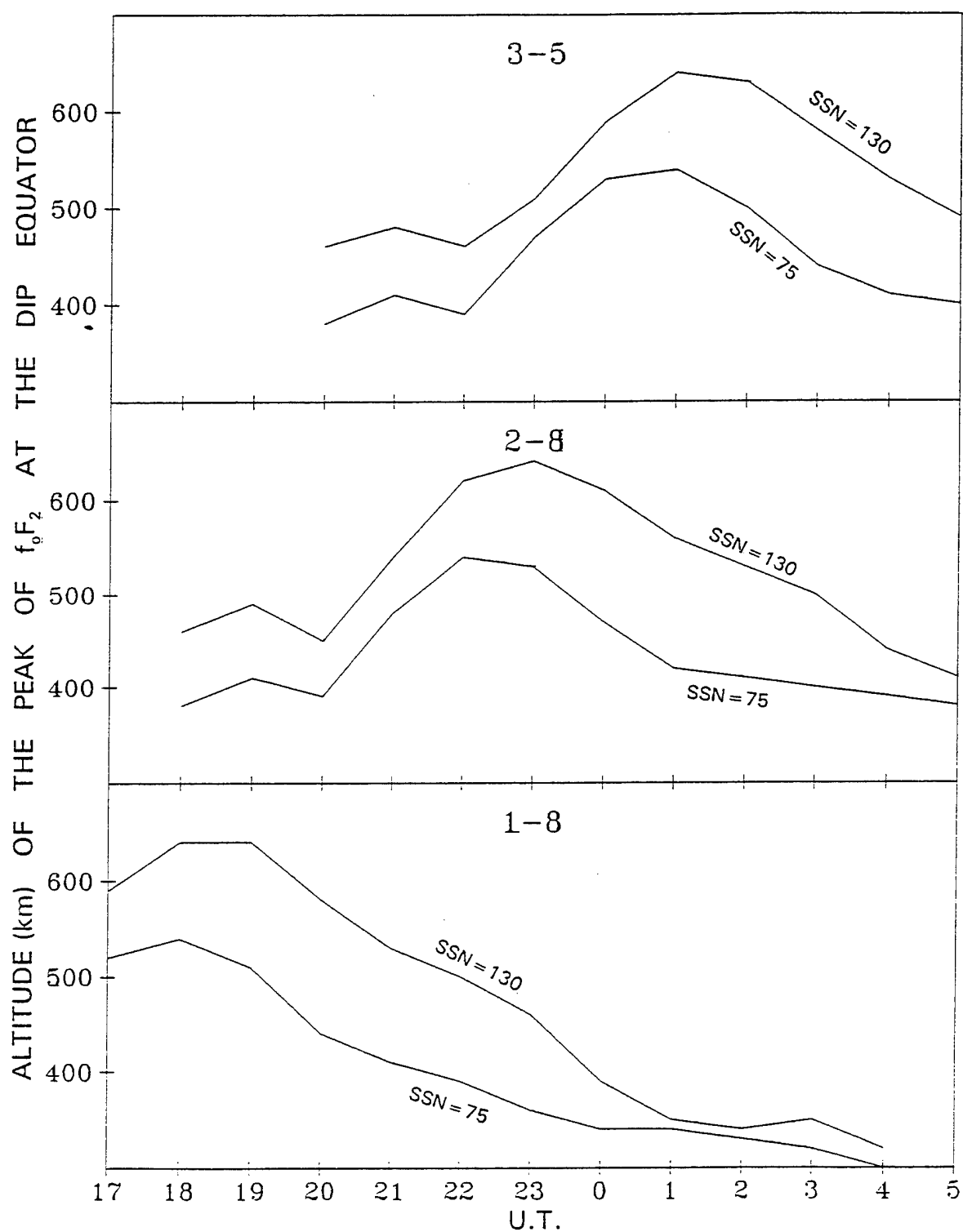
Figure 18. Time dependence of the altitude of peak f_oF_2 at the dip equator in beams 3-5, 2-8 and 1-8 for high and low solar activity (SSN=130 and 75 respectively) period for (winter) day 354.

ORIGIN 44.80°N 292°E   AZIMUTH 136.5°
MONTH DECEMBER   2100 UT   SSN=130   KP=2   Q=2
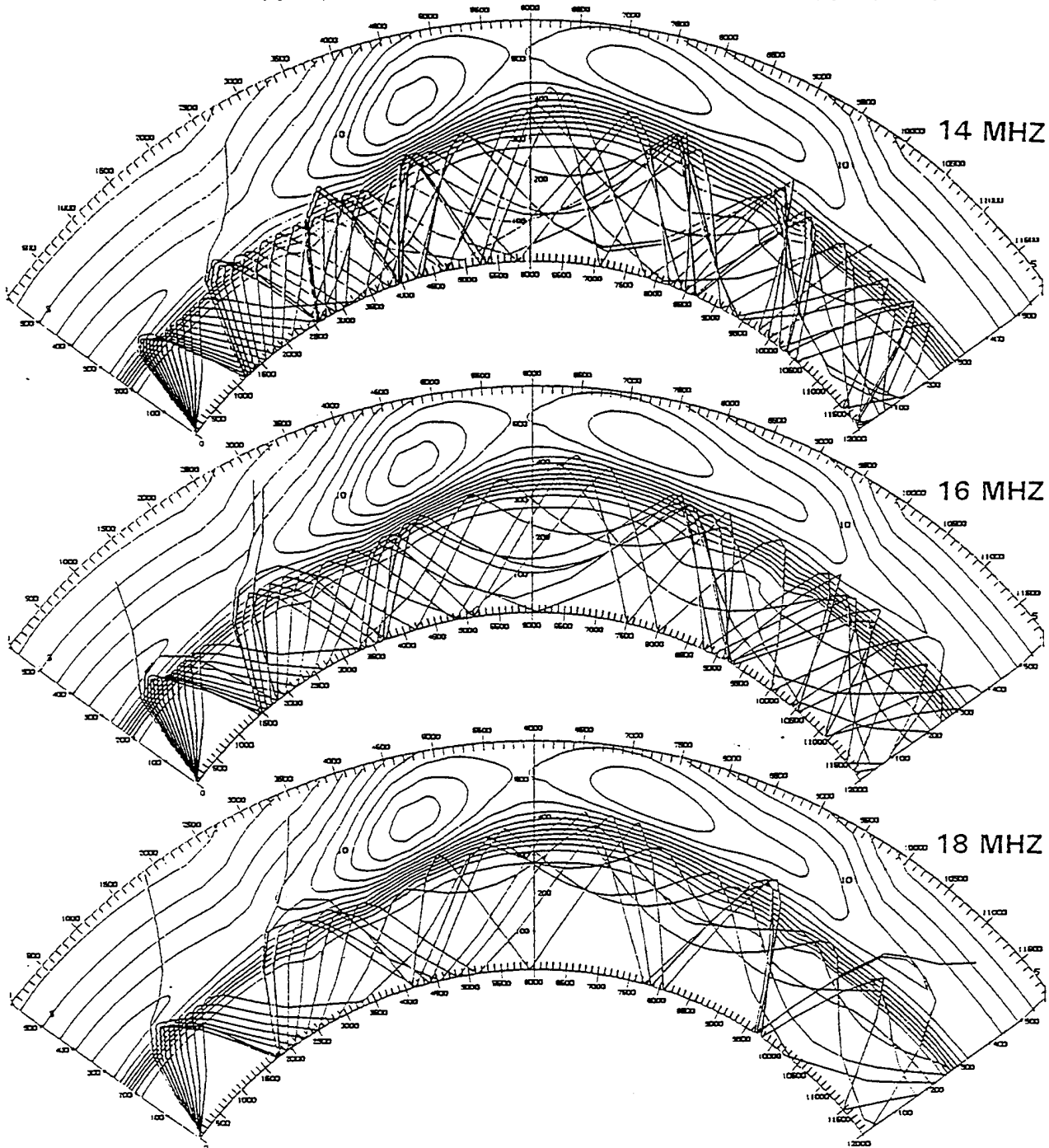
14 MHZ

16 MHZ

18 MHZ

Figure 19. Raytrace for beam 2-8 for (winter) Day 354, SSN=130 for 14, 16 and 18 MHz.

COMPARISON OF IONOSPHERIC MODELS IONCAP AND PIM 1-06
ORIGIN 44.80°N 292°E   AZIMUTH 136.5°
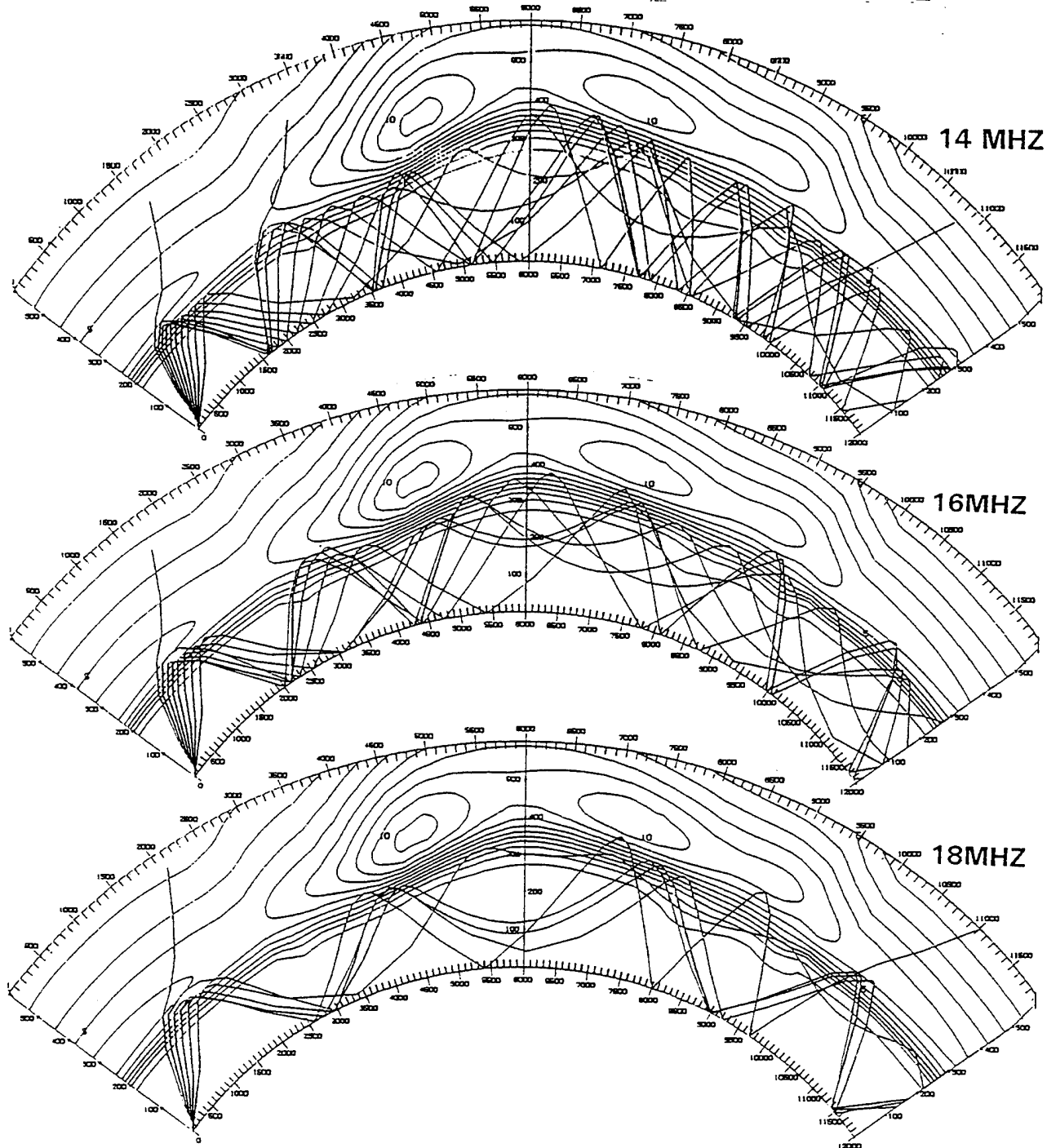MONTH DECEMBER   2100 UT   SSN=75   KP=2   Q=2

Figure 20. Raytrace for beam 2-8 for (winter) Day 354, SSN=75 for 14, 16 and 18 MHz.

SYNTHESIZED BACKSCATTER IONOGRAM

MONTH
DECEMBER

TIME
21:00

LAT   LON
44.8   292.0

AZIM
136.5

SSN   KP
130.0 2.0

ELEV ANG
3.0   29.0
STEP   1.00

MODEL
PIM 1.0.6

RANGE (KM)

FREQUENCY (MHZ)

SYNTHESIZED BACKSCATTER IONOGRAM

MONTH
DECEMBER

TIME
21:00

LAT   LON
44.8   292.0

AZIM
136.5

SSN   KP
75.0   2.0

ELEV ANG
3.0   29.0
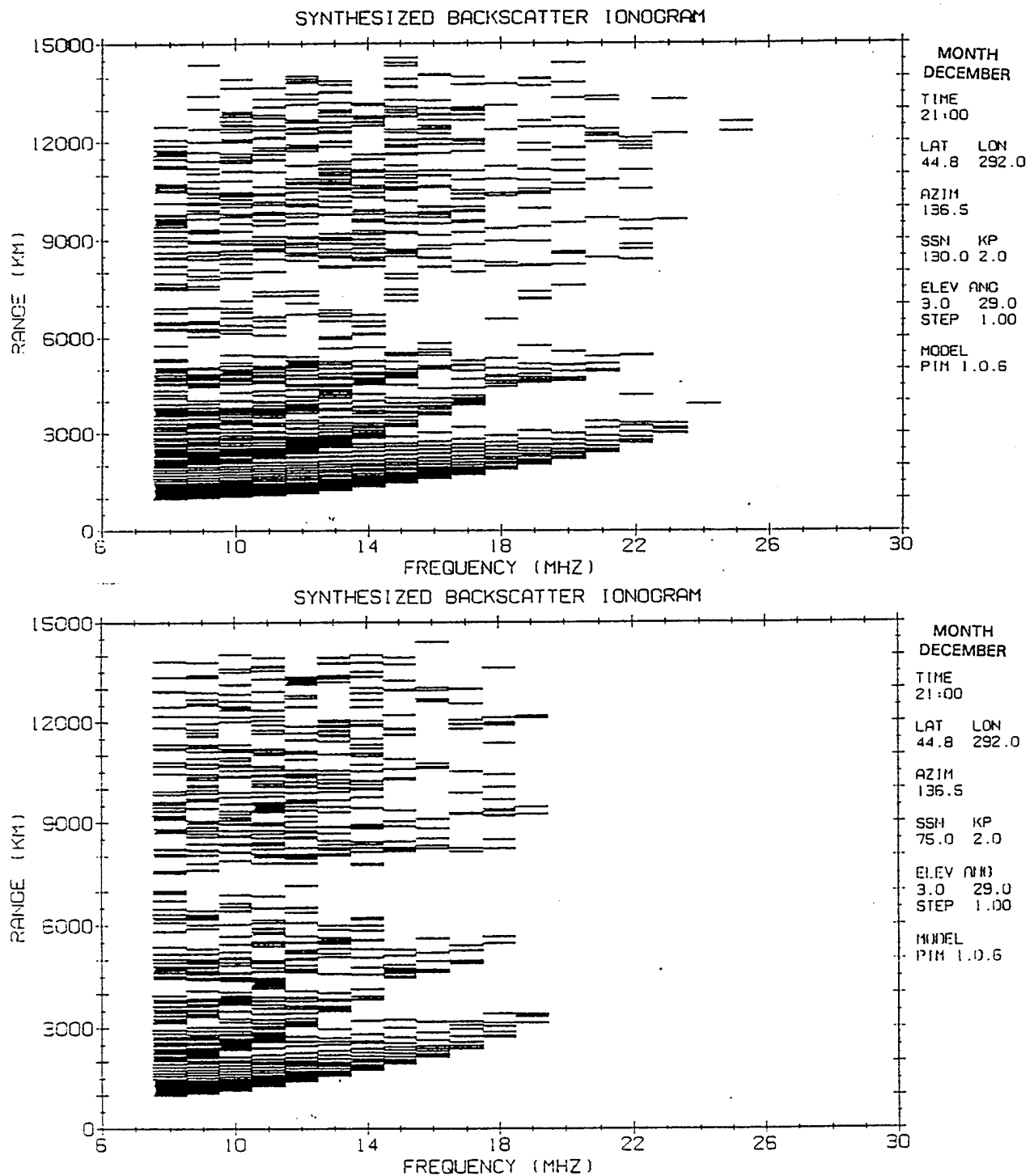STEP   1.00

MODEL
PIM 1.0.6

RANGE (KM)

FREQUENCY (MHZ)

Figure 21. Synthesized Backscatter Ionogram for beam 2-8, (winter) Day 354 for high and low solar (SSN=130 and 75 respectively) activity.

59

ORIGIN 44.80°N 292°E   AZIMUTH 76.5°
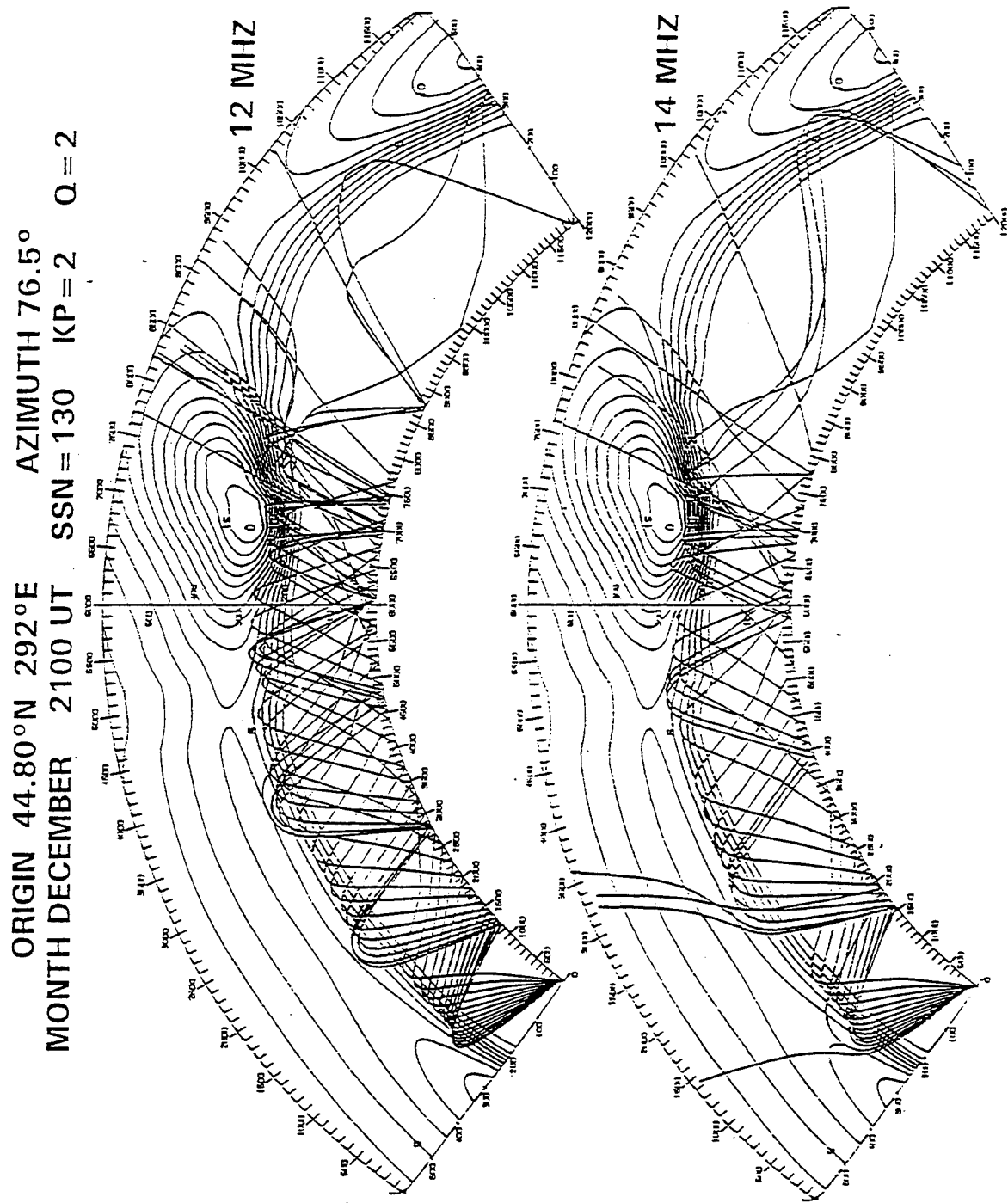MONTH DECEMBER   2100 UT   SSN=130   KP=2   Q=2

12 MHZ

14 MHZ

Figure 22. Raytrace for beam 1-8 for (winter) Day 354, SSN=130 for 12 and 14 MHz.

60

requiring more than 5 F-layer hops to reach the equatorial dome and generating chordal modes as seen in beam 2-8 (in Figures 19 and 20). At these distances the beam power is well attenuated.

In the backscatter ionograms the vertical scale is the time delay, converted to slant range. On the other hand, in the raytrace program we have both parameters: the ground range along the surface of the earth and the actual path distance traversed by the beam. The difference between these two parameters is a function of the operating frequency, the elevation angle, and the number of hops travelled by the beam. All the raytraces of Figures 19-22 were used to determine the relationship of ground range with the difference between slant and ground range shown in Figure 23. The figure shows that a minimum correction from slant range to ground range is 3 percent, and the average correction is 6 percent. For ±2σ levels of the population these corrections are 3.5 percent and 11.5 percent respectively. The figure is useful in estimating ground range from the observed slant ranges in the backscatter ionograms. On the basis of these data, an average correction of 6 percent is used in converting slant range to ground range in Figures 7 and 8.

6. CONCLUSIONS

This data base provides information on the behavior of the equatorial clutter over a local time of 1100 to 0500, a period of about 16 hours. The equatorial clutter is expected to continue through sunrise transition hours (demonstrated by a few cases) but the present data base does not cover the late night period to provide conclusive evidence of this. The clutter occurrence covers a dip latitude range of ±40°. The distance from the radar to the equatorial clutter is longer at high solar activity than at low solar activity. The equatorial clutter occurs less often near the dip equator between 17 and 21 LT. The equatorial clutter typically starts after sunset and continues past midnight.

The use of the raytrace technique shows that essentially the southern part of the equatorial dome of the electron density distribution favors the chordal mode and produces horizontal trace signatures showing clutter of equatorial origin. The wave propagation modes are similar in beams 3-5 and 2-8, which are south and south-east looking beams. For the east looking beam 1-8 the equatorial dome is much further away, therefore the ray path is much longer and the equatorial clutter signatures are much weaker that those seen in beams 3-5 and 2-8.
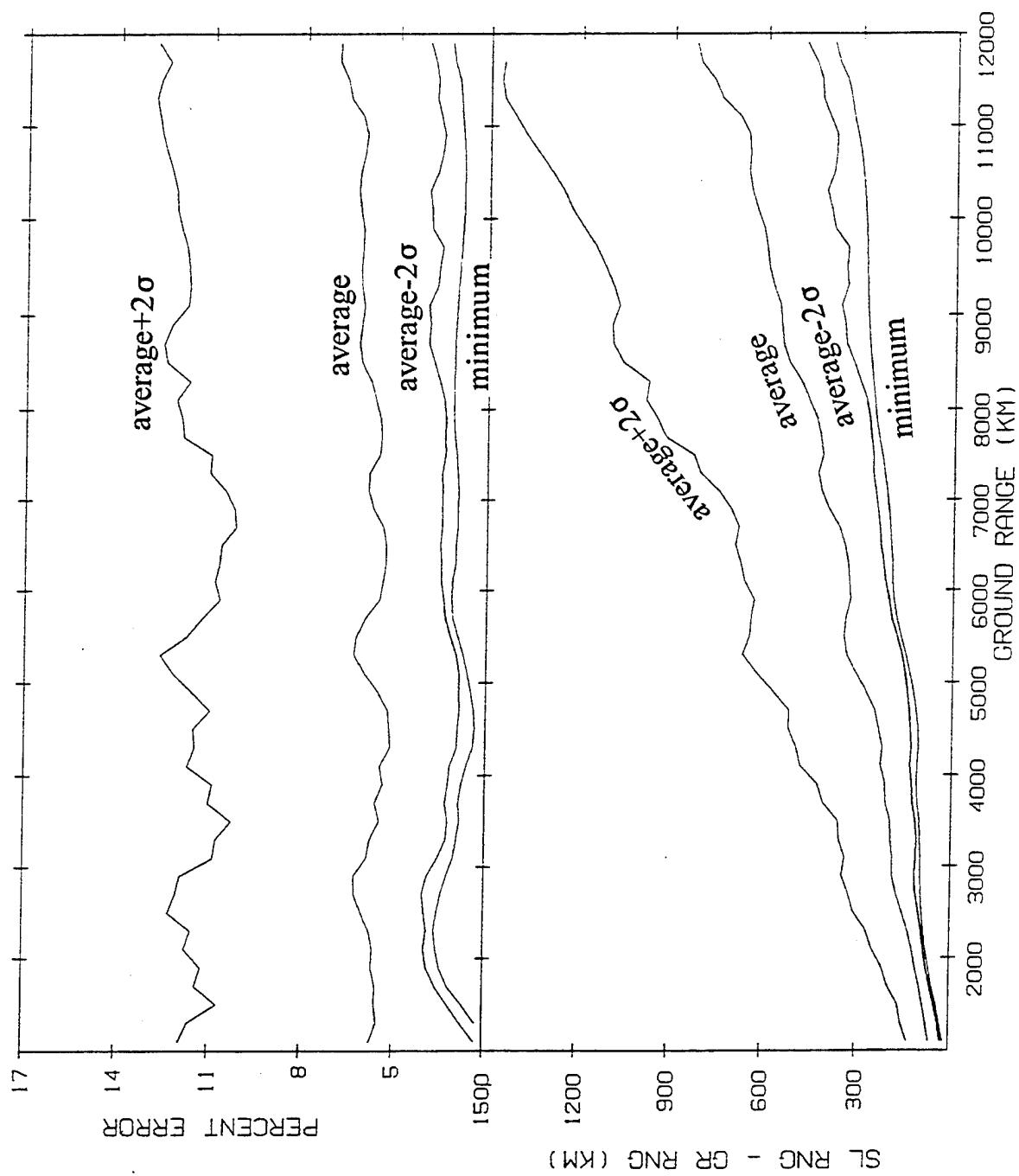
Figure 23. Difference between slant range and ground range as a function of ground range.

References

1. Daniell Jr., R. E., Brown, L. D., Anderson, D. N., Fox, M. W., Doherty, P. H., Decker, D. T., Sojka, J. J., and Schunk, R. W., (1994), Parameterized Ionospheric Model: A global ionospheric parameterization based on first principles models, *Radio Science*, 30:1499-1510.

2. Jones, R. M., and Stephenson, J. J., (1975), *A Versatile Three-Dimensional Ray Tracing Computer Program for Radio Waves in the Ionosphere*, OT Report 75-76, US Department of Commerce, Office of Telecommunications .

3. Lloyd, J. L., Haydon, G. W., Lucas, D. L., and Teters, L R., (1978), *Estimating the Performance of Telecommunication Systems Using the Ionospheric Transmission Channel*, National Telecommunications and Information Administration, Boulder, Colorado.